

IMPACT OF ALKALINE DOPING AND REDUCING CONDITIONS ON LaFeO_3

by

Geoffrey L. Beausoleil II

A thesis

submitted in partial fulfillment

of the requirements for the degree of

Master of Science in Materials Science and Engineering

Boise State University

December 2013

© 2013

Geoffrey L. Beausoleil II

ALL RIGHTS RESERVED

BOISE STATE UNIVERSITY GRADUATE COLLEGE

DEFENSE COMMITTEE AND FINAL READING APPROVALS

of the thesis submitted by

Geoffrey L. Beausoleil II

Thesis Title: Impact of Alkaline Doping and Reducing Conditions on LaFeO_3

Date of Final Oral Examination: 22 August 2013

The following individuals read and discussed the thesis submitted by student Geoffrey L. Beausoleil II, and they evaluated his presentation and response to questions during the final oral examination. They found that the student passed the final oral examination.

Darryl P. Butt, Ph.D. Chair, Supervisory Committee

Alex Punnoose, Ph.D. Member, Supervisory Committee

Rick Ubic, Ph.D. Member, Supervisory Committee

The final reading approval of the thesis was granted by Darryl P. Butt, Ph.D., Chair of the Supervisory Committee. The thesis was approved for the Graduate College by John R. Pelton, Ph.D., Dean of the Graduate College.

DEDICATION

First and foremost I would like to dedicate this thesis to Jesus Christ, for all that he's done and will continue to do in my life. Similarly I would like to dedicate this to my wife, Kaley, and my children, Ellis and Remi, who have been tremendously patient with me and my absences while working on this project. I would also like to dedicate this thesis to all my professors and fellow students who have challenged me to do good work and persevere through the hard times.

Hebrews 12:1 "Therefore, since we are surrounded by so great a cloud of witnesses, let us also lay aside every weight, and sin which clings so closely, and let us run with endurance the race that is set before us."

ACKNOWLEDGEMENTS

There are many people that I would like to acknowledge for contributing in some fashion to the production of this thesis and all of my development as a graduate student. I would first like to acknowledge my advisor and committee, Dr. Darryl Butt, Dr. Alex Punnoose, and Rick Ubic, for their advisement and investment of time and expertise in me as well as the financial support of this research.

I would also like to acknowledge the Nuclear Regulatory Commission for their support of me through their Nuclear Materials Fellowship program, NRC-38-08-955.

I would finally like to acknowledge many of my professors and fellow students, some of which include Dr. Will Hughes, Dr. Josh Kane, Gordon Alanko, Brian Jaques, and Jordan Chess for always being available for me as a friend and colleague, willing to challenge me as a person and scientist and able to keep me grounded and on course.

ABSTRACT

Efficient and reliable materials for gas separation, syngas production, and hybrid nuclear power plants must be capable of reliably operating at a high-temperature range of 700-1000°C and under exposure to highly oxidizing and reducing conditions. Candidate materials for these applications include alkaline metal doped lanthanum ferrite.

In the first study, the impact of A site substitution by different alkaline metals on lanthanum ferrite (LMF, M=Ca, Sr, and Ba) was investigated. The study focused on thermal expansion near the Néel transition temperature and a magneto-elastic contribution to thermal expansion was identified for each sample. Iron oxidation, Fe³⁺ to Fe⁴⁺, was identified as a preferred charge-compensation mechanism for Ca substitution while a mix of iron oxidation and oxygen-vacancy formation was identified for Sr and Ba substituted samples.

The second study focused only on calcium substituted lanthanum ferrite but with a comparison between stoichiometric and sub-stoichiometric quantities of iron on the B site. The samples were heat treated in oxidizing (air), mildly reducing (Ar), and very reducing (5% H₂-N₂) atmospheres to compare the impact of iron sub-stoichiometry and P_{O₂} on the Néel transition and orthorhombic-to-rhombohedral transition temperatures. Treatment in reducing conditions caused the Néel transition temperature to increase for all samples. The orthorhombic-to-rhombohedral transition temperature was determined to decrease for samples treated in Ar and to occur gradually over a broad temperature range

when treated in 5% H₂-N₂. Iron deficiency during preparation was determined to cause a decrease in calcium actual content and a general increase in both phase transition temperatures in all samples. Iron vacancy formation was also determined to be unlikely due to the high energy of the defect and the samples compensated for iron substoichiometry by rejecting calcium on the A site in favor of lanthanum.

TABLE OF CONTENTS

DEDICATION.....	iv
ACKNOWLEDGEMENTS.....	v
ABSTRACT.....	vi
LIST OF TABLES.....	xi
LIST OF FIGURES.....	xii
LIST OF ABBREVIATIONS.....	xiv
CHAPTER ONE: BACKGROUND.....	1
1.1 Structure.....	1
1.1.1 Cubic Structure.....	1
1.1.2 Octahedra Tilting.....	2
1.2 Alkaline Doped Lanthanum Ferrite.....	4
1.2.1 Defects and Distortions.....	4
1.2.2 Non-Stoichiometry.....	6
1.3 Experimental Approach.....	6
1.3.1 Chapter Two.....	7
1.3.2 Chapter Three.....	8
1.4 References.....	9
CHAPTER 2: THERMAL EXPANSION OF ALKALINE-DOPED LANTHANUM FERRITE NEAR THE NÉEL TEMPERATURE.....	12
Abstract.....	13

2.1 Introduction.....	14
2.2 Experimental Procedures	15
2.2.1 Sample Preparation	15
2.2.2 Sample Characterization Methods.....	16
2.3 Results and Discussion	17
2.3.1 X-Ray Diffraction	17
2.3.2 Dilatometry	22
2.3.3 Vibrating Sample Magnetometry.....	25
2.3.4 Neutron Diffraction.....	27
2.4 Conclusions.....	31
2.5 Acknowledgements.....	32
2.6 Author Justifications	32
2.7 References.....	33
CHAPTER THREE: PHASE TRANSITIONS OF $\text{La}_{0.9}\text{Ca}_{0.1}\text{Fe}_y\text{O}_{3-\delta}$ AT LOW OXYGEN PARTIAL PRESSURES.....	37
Abstract.....	39
3.1 Introduction.....	39
3.2. Experimental Methods.....	41
3.2.1 Sample Preparation	41
3.2.2 Characterization Methods	42
3.3 Results and Discussion	43
3.3.1 X-Ray Diffraction	43
3.3.2 Dilatometry	50
3.3.3 TG-DSC/DTA.....	53

3.4 Conclusions.....	57
3.5 Acknowledgements.....	58
3.6 Author Justifications.....	58
3.7 References.....	59

LIST OF TABLES

Table 2.1.	Lattice parameters and volume of each sample determined from XRD and the cell volume determined by the Ubic ²² model.....	18
Table 2.2.	Comparisons of the Néel temperatures found for all samples observed in this study and T_N listed in literature. Komornick and Wattiaux used Thermogravimetric Analysis to determine the Néel Temperature while Fossdal used HT-XRD. ^{4, 15, 16}	24
Table 2.3.	Fe-O1-Fe bond angle, change in T_N from bond angle changes, and moment/ion found through neutron diffraction. The moments are refined along the a-axis and the super exchange of Fe^{3+} -O- Fe^{3+} occurs along the c-axis and corresponds to the Fe-O1-Fe bond angle. The ΔT_N listed is based on the assumption of identical iron content between samples and is determined solely upon the change in the Fe-O1-Fe bond angle.....	28
Table 3.1	Lattice parameters and unit cell volumes of $La_{0.9}Ca_{0.1}Fe_yO_{3-\delta}$ compounds determined by XRD.	50
Table 3.2.	Orthorhombic-to-rhombohedral transition temperatures determined by dilatometry (DIL) and differential scanning calorimetry (DSC) in dry air and argon. The orthorhombic-to-rhombohedral transition measured in 5% H_2-N_2 occurred over a relatively wide temperature range and therefore could not be determined with precision by DSC or dilatometry.	52
Table 3.3.	Néel transition temperatures determined by dilatometry.....	52

LIST OF FIGURES

Fig. 1.1	Ideal cubic perovskite structure of a perovskite.	2
Fig. 1.2	In-phase tilting along the [010] direction (<i>Pnma</i> symmetry) in LaFeO ₃	3
Fig. 1.3	Anti-phase-tilting of octahedra along the [101] direction (<i>Pnma</i> symmetry) in LaFeO ₃	4
Fig. 2.1.	XRD patterns at room temperature for all samples. Patterns are normalized and offset for comparison. Rietveld refinement for LF sample is shown in lower box with cumulative χ^2 and peak indexing.....	18
Fig. 2.2.	Cell volume of samples as determined by Reitveld refined parameters and calculated using Ubic ²² model.	19
Fig. 2.3.	The volume expansion measured by XRD about T _N . The linear, dashed line helps to illustrate the departures from linearity.	21
Fig. 2.4.	Changes in lattice parameters, a, b, and c measured as a function of temperature by HT-XRD. The Néel temperatures are annotated by the drop lines for each sample: LF (upper left), LCF (upper right), LSF (lower left), and LBF (lower right).	22
Fig. 2.5.	Coefficients of thermal expansion measured by dilatometry. The changes in the linearity of the CTE indicate the Néel temperatures, as annotated by the drop lines.....	24
Fig. 2.6.	Magnetometry results showing the Néel temperature (peaks) associated with the anti-ferromagnetic to paramagnetic transformations. The magnetizations are offset and normalized to better illustrate the relative changes in T _N	26
Fig. 2.7.	The <i>Pbnm</i> structure of LaFeO ₃ . The O1 site oxygen atoms shown in white are located at the vertices of the FeO ₆ octahedra and are aligned along the long c-axis. The large A site cations are shown in green. The iron cations are shown in the center of the octahedra.....	30
Fig 3.1.	a) Full XRD patterns of as-prepared samples and b) the high-angle patterns to highlight the peak positions. B) Rietveld refinement calculated line and observed points to show an example of the refinements done....	44

Fig 3.2.	Concentrations of La, Ca, Fe and La/Ca ratio of as-prepared samples determined by EDS (solid squares) and XPS (solid circles). EDS points were determined by the mean of 20+ scans with a 95% confidence.	45
Fig. 3.3.	Lattice parameters and cell volume of all samples determined from Rietveld refinement. The b parameter is described by the ratio $b_{\text{shown}}=b_{\text{actual}}/\sqrt{2}$	46
Fig. 3.4.	XRD patterns for samples exposed to designated atmosphere at 1100°C. Column a) shows the entire XRD pattern with asterisk annotating some of the super-lattice reflections. Column b) shows the high angle data with drop lines to highlight the slight shift of peaks to lower angles with decreasing iron content.	48
Fig. 3.5.	Coefficient of thermal expansion (CTE) plots for all three atmosphere treatments with a +1 offset between compositions to more clearly show distinction between compositions. The Néel transition (T_N) is annotated for each sample. The orthorhombic-to-rhombohedral transition is annotated for air and Ar runs but was not observable for the 5% H_2-N_2 treated samples. Different T_N s were observed for each composition in air- and Ar- treated samples. No difference in T_N was observed for any composition in the 5% H_2-N_2 treatment. All transition temperatures annotated here are listed in Tables 3.1 and 3.2.	51
Fig. 3.6.	T_{OR} in air and Ar was determined by the position of the endothermic peak in the DSC data and is annotated on the graph (left column). The right column shows the TG data for both air and Ar and has the Néel and O-R transitions annotated to show mass losses about the transitions.....	54
Fig. 3.7.	TG-DTA data for samples treated in 5% H_2-N_2 . Neither the Néel nor T_{OR} could be identified from the DTA data. A significant mass loss occurs and ends at the T_N determined from dilatometry and corresponds to a complete oxidation of Fe^{4+} to Fe^{3+} and some Fe^{3+} becoming Fe^{2+}	55
Fig. 3.8.	Total mass loss over the Néel transition for samples in 5% H_2-N_2 . The mass loss for non-stoichiometric samples is suggests that the iron is already reduced and that the T_N for non-stoichiometric samples should be higher than for stoichiometric samples.	56
Fig. 3.9.	Decomposition mass loss for samples in 5% H_2-N_2 . The increasing magnitude of mass loss confirms that there was less oxygen available for non-stoichiometric samples and there were more intrinsic oxygen defects in the samples compared to stoichiometric samples.	56
Fig. 3.10.	Time to decomposition for samples held at 1100°C showing that non-stoichiometric samples are more stable and stoichiometric samples.....	57

LIST OF ABBREVIATIONS

BSU	Boise State University
GC	Graduate College
TDC	Thesis and dissertation coordinator
LF	Lanthanum ferrite
LCF	$\text{La}_{0.9}\text{Ca}_{0.1}\text{FeO}_3$
LSF	$\text{La}_{1-x}\text{Sr}_x\text{FeO}_3$
LBF	$\text{La}_{1-x}\text{Ba}_x\text{FeO}_3$
AFM	Anti-ferromagnetic
T_N	Néel temperature
T_{OR}	Orthorhombic-to-rhombohedral transition temperature
O-R	Orthorhombic-to-rhombohedral transition
XRD	X-ray diffraction
SEM	Scanning electron microscopy
EDS	Electron dispersive spectroscopy
VSM	Vibrating sample microscopy
ND	Neutron diffraction

UHP	Ultra-high purity
TG(A)	Thermogravimetric (analysis)
DSC	Differential scanning calorimetry
DTA	Differential thermal analysis
DIL	Dilatometry
CTE	Coefficient of thermal expansion
VSM	Vibrating sample magnetometry
P_x	Partial pressure of a gas (x)
RP	Ruddlesden-Popper Phase
IPA	Isopropyl Alcohol

CHAPTER ONE: BACKGROUND

1.1 Structure

The perovskite structure is named after the crystal structure of the perovskite mineral, CaTiO_3 . The term perovskite refers to a large number of compositions that exist with the same structure. A perovskite is chemically described by ABX_3 , where the A and B denote two cation sites and the X denotes the anion site. In most cases, the X position is occupied by an oxygen atom and so the perovskite is commonly described as ABO_3 . The B site cation has 6-fold coordination with the anions and form BO_6 octahedra. The A site cation ideally has 12-fold coordination and the anion has 2-fold coordination.

1.1.1 Cubic Structure

The ideal perovskite is a cubic structure and can be described with the A site cation existing on the corners of the cell with a BX_6 octahedra resting in the middle of the cell (Fig. 1).¹ However, most perovskite materials exist in a pseudo-cubic state due to distortions in orientation and position of the BX_6 octahedra. Two of the most prominent structures for perovskites have orthorhombic and tetragonal symmetries where the octahedra tilt in at least one crystallographic direction.² In most pseudo-cubic perovskites, the A site coordination maintains its 12-fold coordination. The anion generally maintains its 2-fold coordination in pseudo-cubic structures.

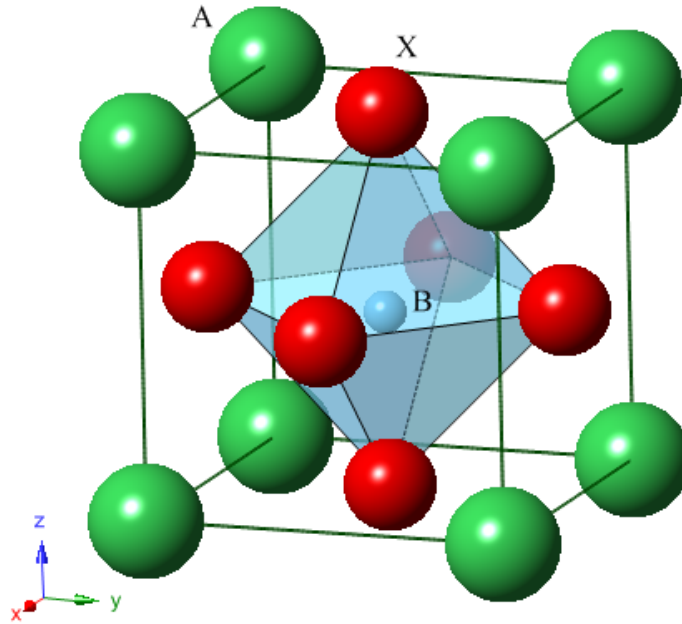


Fig. 1.1 Ideal cubic perovskite structure of a perovskite.

1.1.2 Octahedra Tilting

The primary cause for distortions to the cubic perovskite structure is octahedra tilting. There are two types of octahedra tilting, in-phase and anti-phase tilting. In-phase tilting is when the octahedra tilt in unison along an axis and is shown in Fig. 2. Anti-phase tilting is when the octahedra tilt in alternating directions along an axis and is shown in Fig. 3. Lanthanum ferrite has in-phase tilting along the b-axis and anti-phase tilting along the a and c axes.³ The distortion caused by the tilting produces an elongation of the b-axis such that $a \sim c$ and $\sqrt{2}a \sim b$.

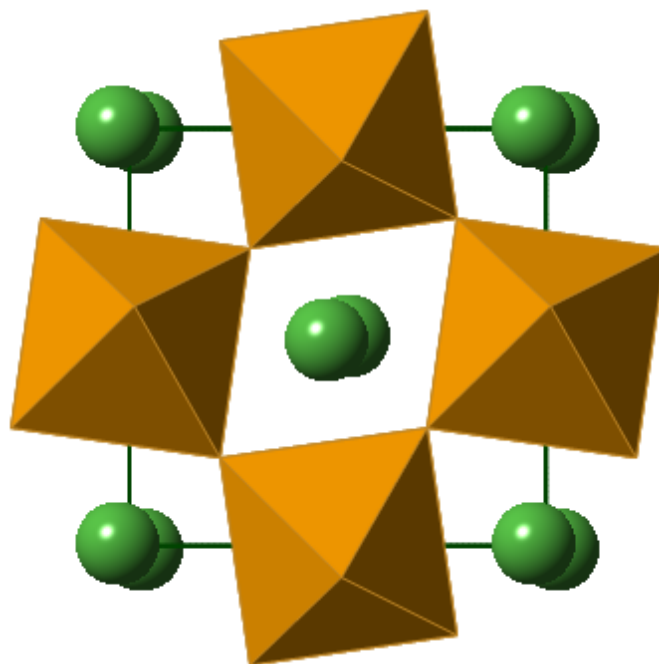


Fig. 1.2 In-phase tilting along the [010] direction (*Pnma* symmetry) in LaFeO₃.

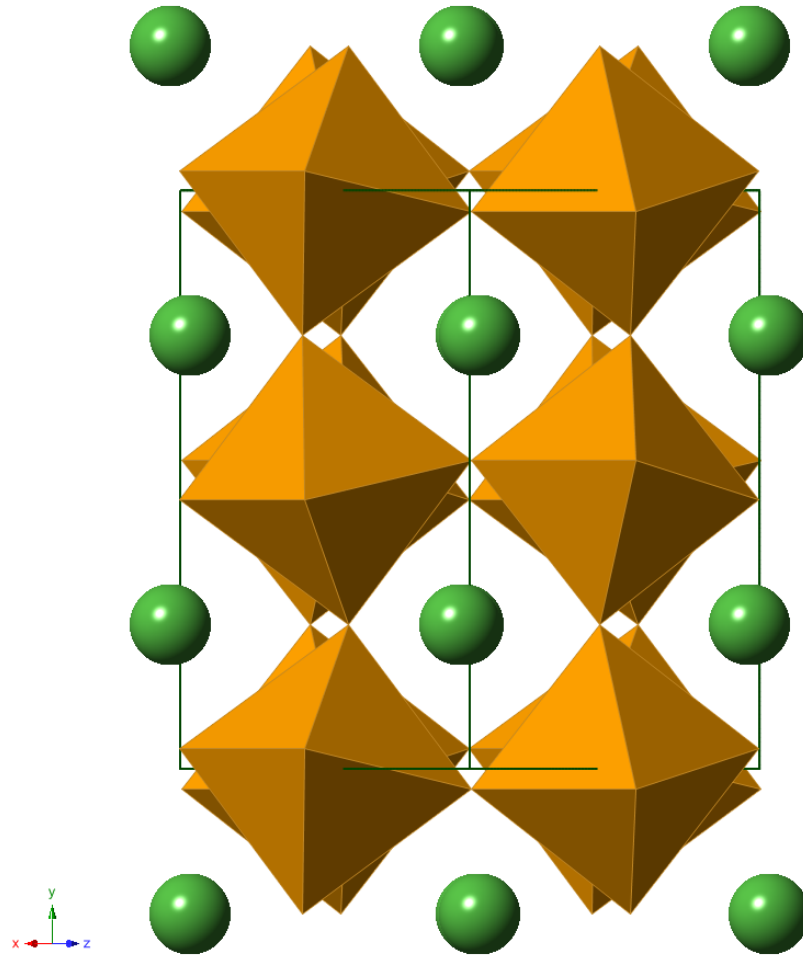


Fig. 1.3 Anti-phase-tilting of octahedra along the [101] direction (*Pnma* symmetry) in LaFeO_3

1.2 Alkaline Doped Lanthanum Ferrite

Alkaline metal doped lanthanum ferrite (LMF, $M=\text{Ca, Sr, Ba}$) is an orthorhombic perovskite with *Pnma* symmetry (space group #62, also often called *Pbnm*).^{4, 5} The alkaline cation substitutes on the A site in place of a lanthanum cation.

1.2.1 Defects and Distortions

When an alkaline cation is substituted for lanthanum, there must be some compensation for the charge difference between M^{2+} and La^{3+} by either the oxidation of

iron from Fe^{3+} to Fe^{4+} or the formation of an oxygen-vacancy. Previous research has shown that for low concentrations of Ca, such as 10%, the primary mechanism for charge-compensation is the oxidation of iron and that a significant number of oxygen vacancies do not form except under reducing conditions;^{6, 7} however, there is less agreement on the charge-compensation mechanism for LF with Sr or Ba substitutions.^{3, 8}

In either case, both charge-compensation mechanisms cause significant changes to the LF system. The oxidation of iron causes a significant change for two reasons. The first reason is that the ionic radius of Fe^{4+} is $r = 0.725\text{\AA}$ and the ionic radius of high-spin Fe^{3+} is $r = 0.785\text{\AA}$, which causes a contraction of the unit cell.⁹ If a large number of oxygen vacancies are formed to compensate for charge differences, then the cell may also increase since the relative charge of the vacancy will cause a Coulombic repulsion between neighboring cations and the positive charge of the vacancy. However, when the coordination of Fe^{3+} decreases from 6 to 5 or 4, the ionic radius decreases to 0.72 and 0.639 \AA , respectively, decreasing the unit cell. If there is a small number of oxygen vacancies formed, then the unit cell could also experience a relaxation around the vacancy site and decrease in size.

In addition to the changes caused by charge-compensation, the dopants cause changes to the size of the unit cell as well. The substitution of La with Ca causes little change in the structure since the ionic radii of each are about the same ($r_{\text{Ca}} = 1.48\text{\AA}$ and $r_{\text{La}} = 1.50\text{\AA}$), while the substitution of Sr or Ba causes a measureable increase in size for the structure ($r_{\text{Sr}} = 1.58\text{\AA}$ and $r_{\text{Ba}} = 1.75\text{\AA}$).⁹

1.2.2 Non-Stoichiometry

There has been very little research on B site deficient perovskites with La as an A site cation, but B site deficient perovskites have been widely studied for a number of different compositions. The few studies that have been done on B site deficient perovskites involved A site cations other than lanthanum.^{10, 11} In these studies, the effect of B site deficiency on structure was investigated and a secondary phase called a Ruddseden-Popper (RP) phase was identified. However, the RP phase can be ruled out for perovskite systems with La on the A site and iron on the B site due to geometric limitations.¹²

While research has suggested that the formation of B site vacancies could occur, it is important to note that the formation of an iron vacancy is highly energetic due to the large relative charge of the vacancy. The relative charge of an iron vacancy in LF is -3 and has 6-fold coordination with oxygen anions that each have a -2 charge. The close proximity of negative charges around the vacancy results in a very strong Coulombic repulsion and causes a very large amount of strain within the system. Due to the high energy of this defects it is not very likely to form and some other mechanism to compensate for the non-stoichiometry must occur.

1.3 Experimental Approach

For the experiments performed in the research presented in this paper, samples were produced using a multi-step solid-state reaction with batch sizes of at least 30 g to ensure a molar variance of ± 0.00005 moles. The powders were then analyzed using X-ray diffraction (XRD) to verify the crystal structure of each material. The powders used for experiments comparing the effect of atmospheric conditions were pressed into pellets

with 30% mass cellulose and annealed at 1100°C to form porous pellets. The powders were left as prepared for experiments that required powdered form, such as XRD and vibrating sample magnetometry.

1.3.1 Chapter Two

There are two studies included in this paper. The first study is on the impact of alkaline substitutions on the A site of LaFeO_3 on thermal expansion near the Néel transition temperature. The Néel transition is the magnetic transition of an anti-ferromagnetic (AFM) material to a paramagnetic material. At room temperature, LaFeO_3 has an anti-ferromagnetic magnetic structure that originates from a super-exchange interaction that occurs between iron ions through an adjoining oxygen ion ($\text{Fe}^{3+}\text{-O-Fe}^{3+}$). Super-exchange interactions occur via the coupling of electrons from two identical cations to the spin of the intermediate non-magnetic anion. In the case of LaFeO_3 , the unpaired d-electron of each Fe^{3+} couples to the spin of one of the electrons from the adjoining oxygen.¹³ An important feature in LaFeO_3 is that the iron cation has 6-fold coordination and could theoretically participate in an exchange in any of the three directions; however, it has been shown using neutron diffraction that the exchange direction is along the long axis of the orthorhombic cell (b for $Pnma$, c for $Pbnm$).⁵ As a result, the iron ions form magnetic moments perpendicular to the exchange direction, which lies somewhere within the $Pnma$ a-c plane. The moments align anti-parallel to each other and the resulting net moment of the system is zero for an ideal AFM lanthanum ferrite system.

Previous research has shown that there are strong interactions between magnetic susceptibility, thermodynamic quantities, and thermal expansion. The magnetic heat

capacity and energy of formation has been researched by Paride *et al.*¹⁴ and Stølen *et al.*¹⁵ and matched to the Néel transition temperature (T_N). Heat capacity also has a very direct relationship to thermal expansion and other properties. Due to the magnetic contribution to heat capacity, there is an indirect magnetic contribution to thermal expansion.^{3, 16, 17} Chapter Two will investigate the impact that substituting lanthanum cations with alkaline metal cations has on the Néel temperature, thermal expansion, and the relationship between the two using a combination of high-temperature XRD, dilatometry, vibrating sample magnetometry, and neutron diffraction

1.3.2 Chapter Three

The second study included within this text is on phase transitions of B site deficient calcium doped lanthanum ferrite (LCF) in high-temperature reducing conditions. As a candidate material for high-temperature applications such as syngas production, the changes in phase transition temperatures and impact of non-stoichiometry is of significant interest.^{18, 19} The orthorhombic-to-rhombohedral (O-R) transition temperature (T_{OR}) for pure LF is known to be around 1000°C, which is above the operating temperatures of proposed applications, but T_{OR} is not known for LCF or non-stoichiometric samples. In addition, most proposed applications require exposure to both oxidizing and reducing conditions at high-temperatures. The extreme concentration gradient of oxygen between surfaces has the potential to cause significant and permanent changes to the composition and structure of the materials and significantly compromise performance.

This study focused on compositions of $\text{La}_{0.9}\text{Ca}_{0.1}\text{Fe}_y\text{O}_{3-\delta}$ for $y=1.000, 0.995,$ and 0.990 and compared heat treatments of each sample in oxidizing and reducing conditions.

A suite of XRD, dilatometry, and thermal analysis (TG-DSC/DTA) was used to characterize the materials and establish T_N and T_{OR} for each composition and atmospheric condition.

1.4 References

1. C. B. Carter and M. G. Norton, *Ceramic Materials: Science and Engineering*, 2nd ed.; Ch. Chapter. Edited. Springer: New York, 2013.
2. K. S. Aleksandrov, "The Sequences of Structural Phase Transitions in Perovskites," *Ferroelectrics*, **14** [3-4] 801-05 (1976).
3. S. Komornicki, L. Fournes, J. C. Grenier, F. Menil, M. Pouchard, and P. Hagenmuller, "Investigation of Mixed Valency Ferrites $La_{1-x}Ca_xFeO_{3-y}$ ($0 \leq x < 0.50$) With the Perovskite Structure," *Materials Research Bulletin*, **16** [8] 967-73 (1981).
4. J. M. Hudspeth, G. A. Stewart, A. J. Studer, and D. J. Goossens, "Crystal and Magnetic Structures in Perovskite-related $La_{1-x}Ca_xFeO_3$ ($x = 0.2, 0.33$)," *Journal of Physics and Chemistry of Solids*, **72** [12] 1543-47 (2011).
5. P. Ciambelli, S. Cimino, L. Lisi, M. Faticanti, G. Minelli, I. Pettiti, and P. Porta, "La, Ca and Fe Oxide Perovskites: Preparation, Characterization and Catalytic Properties for Methane Combustion," *Applied Catalysis B-Environmental*, **33** [3] 193-203 (2001).
6. H. Taguchi, Y. Masunaga, K. Hirota, and O. Yamaguchi, "Synthesis of Perovskite-type $La_{1-x}Ca_xFeO_3$ ($0 \leq x < 0.2$) at low temperature," *Materials Research Bulletin*, **40** [5] 773-80 (2005).
7. M. Ghaffari, T. Liu, H. Huang, O. K. Tan, and M. Shannon, "Investigation of Local Structure Effect and X-ray Absorption Characteristics (EXAFS) of Fe (Ti) K-edge

- on Photocatalyst Properties of $\text{SrTi}_{(1-x)}\text{Fe}_x\text{O}_3$," *Materials Chemistry and Physics*, **136** [2-3] 347-57 (2012).
8. S. M. Selbach, J. R. Tolchard, A. Fossdal, and T. Grande, "Non-linear Thermal Evolution of the Crystal Structure and Phase Transitions of LaFeO_3 Investigated by High-temperature X-ray Diffraction," *Journal of Solid State Chemistry*, **196** 249-54 (2012).
9. R. D. Shannon, "Revised Effective Ionic-Radii and Systematic Studies of Interatomic Distances in Halides and Chalcogenides," *Acta Crystallographica Section A*, **32**[SEP1] 751-67 (1976).
10. M. Mori and Z. W. Wang, "Pore Formation During Sintering Process of $(\text{Sr}_{0.9}\text{La}_{0.1})_{1-x}\text{Ti}_{1-y}\text{O}_{3+\delta}$ Perovskites ($x, y = 0, 0.04$) Synthesized by the Citric Acid Method," *Electrochemistry*, **78** [11] 896-99 (2010).
11. M. Mori, Z. W. Wang, T. Itoh, S. Yabui, K. Murai, and T. Moriga, "A site and B site Non-stoichiometry and Sintering Characteristics of $(\text{Sr}_{1-x}\text{La}_x)_{1-y}\text{Ti}_{1-z}\text{O}_3$ Perovskites," *Journal of Fuel Cell Science and Technology*, **8** [5] 4 (2011).
12. B. Beznosikov and K. Aleksandrov, "Perovskite-like crystals of the Ruddlesden-Popper series," *Crystallography Reports*, **45** [5] 792-98 (2000).
13. G. F. Dionne, "Magnetic Oxides" Springer. New York. 2009, pg 15
14. S. C. Parida, S. K. Rakshit, S. Dash, Z. Singh, R. Prasad, and V. Venugopal, "Thermodynamic properties of quaternary oxides in the system Ba-La-Fe-O by differential scanning calorimetry and solid-state electrochemical cells," *Journal of Chemical Thermodynamics*, **36** [10] 911-17 (2004).

15. S. Stolen, F. Gronvold, H. Brinks, T. Atake, and H. Mori, "Heat capacity and thermodynamic properties of LaFeO_3 and LaCoO_3 from $T = 13 \text{ K}$ to $T = 1000 \text{ K}$," *Journal of Chemical Thermodynamics*, **30** [3] 365-77 (1998).
16. L. C. Bartel, "Calculation of Near Neighbor Spin Correlation Functions in MNO and Alpha-MNS for T Less Than T_N ," *Bulletin of the American Physical Society*, **15** [3] (1970).
17. L. C. Bartel, "Magnetic Contribution to Thermal Expansion in an Itinerant Antiferromagnet," *Journal of Applied Physics*, **41** [13] (1970).
18. P. N. Dyer, M. F. Carolan, D. P. Butt, R. M. P. H. van Doorn, R. A. Cutler, and K. D. Gourley, "Mixed Conducting Membranes for Syngas Production," Australia Patent #2001295502. 2005.
19. M. F. Carolan, P. N. Dyer, R. M. P. H. van Doorn, R. A. Cutler, and D. P. Butt, "Ion Transport Membranes for Syngas Production," U.S. Patent #6492290. 2003.

CHAPTER 2: THERMAL EXPANSION OF ALKALINE-DOPED LANTHANUM
FERRITE NEAR THE NÉEL TEMPERATURE

This chapter has been submitted for publication to Wiley in *Journal of American Ceramic Society* and should be referenced appropriately.

Reference:

G. L. Beausoleil II, P. Price, D. Thomsen, Alex Punnoose, R. Uvic, S. Misture, D. P. Butt. *Thermal Expansion of Alkaline-Doped Lanthanum Ferrite Near the Néel Temperature*. J. Am. Cer. Soc., (accepted) 2013

*This chapter includes modifications from the originally submitted version.

**Thermal Expansion of Alkaline-Doped Lanthanum Ferrite
Near the Néel Temperature**

Geoffrey L. Beausoleil II¹

Patrick Price¹

David Thomsen¹

Alex Punnoose²

Rick Ubic^{1,3}

Scott Misture⁴

Darryl P. Butt,^{1,3,*}

¹Department of Materials Science & Engineering and ²Department of Physics, Boise State University, Boise, ID 83725

³Center for Advanced Energy Studies, Idaho Falls, ID 83401

⁴Kazuo Inamori School of Engineering, Alfred University, Alfred, NY 14802

Abstract

The thermal expansion and magnetic behaviors of divalent, alkaline-doped lanthanum ferrites ($\text{La}_{0.9}\text{M}_{0.1}\text{FeO}_3$, M=Ca, Sr, Ba) were assessed using a combination of dilatometry, magnetometry, time-of-flight neutron diffraction, and high-temperature x-ray diffraction. Néel temperatures were determined through vibrating sample magnetometry and correlated well with changes in thermal expansion behavior observed during both dilatometry and x-ray diffraction. The Néel temperatures observed for pure, Ca-doped, Sr-doped, and Ba-doped lanthanum ferrites were 471, 351, 465, and 466°C, respectively. The effect of divalent substitutions on the magnetic behavior are attributed to charge-compensation mechanisms and structural changes in the material.

2.1 Introduction

Divalent cation-doped lanthanum ferrite materials ($\text{La}^{3+}_{1-x}\text{M}^{2+}_x\text{FeO}_{3-\delta}$) exhibit a variety of useful properties including multi-ionic conductivity and multi-ferroic behavior.¹ These materials have been suggested as candidates for high-temperature electrochemical devices such as oxygen-conducting membranes for use in synthesis gas (syngas) or oxygen production, solid-oxide fuel-cell cathodes, and as catalysts for the oxidation of hydrocarbons.^{2,3} Consequently, it is important to understand structural and magnetic phase transformations that may occur at elevated temperatures in order to optimize the performance and reliability of commercial devices.

Lanthanum ferrite (LaFeO_3 , LF) is an orthorhombic (*Pbnm*) perovskite with a canted, G-type anti-ferromagnetic (AFM) structure and undergoes a transition to a paramagnetic state above the Néel temperature ($T_N \approx 477^\circ\text{C}$).⁴ The AFM behavior in LF is caused by spin coupling of iron ions via a super-exchange interaction through an adjoining oxygen atom (Fe-O-Fe). Previous studies have shown a correlation between anti-ferromagnetic behavior, the Néel temperature, and thermal expansion in various perovskite systems.⁵⁻⁸ Selbach *et al.*⁹ demonstrated the existence of magnetic contributions to thermal expansion behavior in LF. Their results show that the Néel temperature can be observed indirectly through thermal expansion measurements due to non-linear thermal expansion caused by magnetoelastic coupling and thermally induced spin excitations that increase the Pauli repulsion.⁹⁻¹¹

Despite their technological relevance, magnetic contributions to thermal expansion behavior of divalent substituted lanthanum ferrites have not yet been reported in the open literature. Substitution of divalent cations on the trivalent lanthanum A site

creates a charge imbalance, which requires compensation through either the formation of oxygen vacancies or an increase in the iron valence from Fe^{3+} to Fe^{4+} .^{12, 13} Although it is possible for Fe^{4+} to disproportionate into a mixture of Fe^{3+} and Fe^{5+} in orthoferrite systems, this has only been observed below 200 K.^{14, 15} In addition to electronic and chemical changes, the different ionic radii of cation substitutions will affect the local structure of the material. Previous studies have reported that divalent cation substitutions in LSF and LCF cause a reduction in the Néel temperatures to approximately 390°C for LSF ($x=0.1$)^{4, 16} and 277°C for LCF ($x=0.2$).^{15, 17}

In this study, the alkaline metals Ca^{2+} , Sr^{2+} , and Ba^{2+} were substituted for La^{3+} on the A site in order to produce samples with the composition $\text{La}_{0.9}\text{M}_{0.1}\text{FeO}_3$ ($\text{M}=\text{Ca}, \text{Sr}, \text{Ba}$). The impact of divalent cation substitutions on the Néel temperature, thermal expansion, and magnetic behavior is shown using a combination of high-temperature x-ray diffraction, time-of-flight neutron diffraction, dilatometry, and magnetometry.

2.2 Experimental Procedures

2.2.1 Sample Preparation

Divalent-cation-doped lanthanum ferrite materials were synthesized via multi-step solid-state reactions under oxidizing conditions in air using the precursor powders La_2O_3 (99.99% purity; Alfa Aesar, Ward Hill MA, United States), Fe_2O_3 (99.995%; Alfa), CaCO_3 (99.995%; Alfa), SrCO_3 (99.995%; Alfa), and BaCO_3 (99.997%; Alfa). Due to their hydrophilic nature, the adsorbed gas contents of the powders were measured using thermogravimetric analysis and compensated for immediately prior to batching. Batch sizes were at least 30 g in order to ensure a molar variance of no greater than ± 0.00005

moles during the weighing process. Precursor powders were milled with yttria-stabilized zirconia media and isopropyl alcohol (IPA) in polymer jars for 12 hours on a table-top mixer and were subsequently calcined at 1000°C for 6 hours in a box furnace. The calcined powders formed a cake-like compact that was subsequently crushed and milled as described above for an additional 10 hours. The calcined mixture was dried and isostatically pressed into green pellets. The pellets were sintered at 1350°C for 24 hours for densification. Once the sintering was complete, a few of the pellets were crushed using a mortar and pestle and ball milling to an approximately 1-2 μm particle size for powder diffraction and magnetic characterization.

2.2.2 Sample Characterization Methods

The *Pbnm* orthorhombic structure of synthesized samples was verified using a Bruker (5465 East Cheryl Parkway, Madison WI 53711, USA) AXS D8 x-ray diffractometer (XRD) with parallel beam geometry at room temperature. The expansion behavior was characterized by high-temperature XRD (HT-XRD) using a Siemens (Karlsruhe, Germany) D5000 XRD with Bragg Brentano geometry between room temperature and 600°C. Atomic bond angles and magnetic moments were characterized with neutron diffraction on the SMARTS beam line at Los Alamos National Laboratory. Diffraction data from XRD and neutrons were analyzed using the Rietveld method and the General Structure Analysis System (GSAS) code with the EXPGUI graphical user interface.^{18, 19}

Thermal expansion behavior was further measured by dilatometry using a Netzsch (129 Middlesex Turnpike, Burlington MA 01803) model 402E with an alumina standard supplied by Netzsch. Dilatometry samples were cut into 25 mm long rods from sintered

pellets and were heated during dilatometry at 10°C/min from room temperature to 1000°C in certified dry air (80% N₂-20% O₂).

The Néel temperature was measured by vibrating sample magnetometry (VSM) with a Lake Shore 7404 VSM (575 McCorkle Blvd, Westerville OH 43082). Samples were loaded into a pre-tested, non-magnetic boron-nitride sample holder and magnetization was measured as a function of temperature in 5°C increments in a resistive heated tube furnace under a field of 0.5 T.

2.3 Results and Discussion

2.3.1 X-Ray Diffraction

Alkaline substituted lanthanum ferrite samples were fabricated with nominal stoichiometry of La_{0.9}M_{0.1}FeO_{3-δ} (M=Ca, Sr, Ba; sample code LMF). The powder XRD patterns for sintered samples are shown in Fig. 2.1 and exhibit the expected orthorhombic structure (*Pbnm*, #62). None of the three compounds, LF, LCF, nor LSF showed any secondary XRD peaks; however, there was a minor peak observed in the LBF pattern at about 31° 2θ, which can be attributed to the minor impurity, BaLa₂Fe₂O₇ and is anti-ferromagnetic with a Néel temperature well below that of LaFeO₃, thus it is not expected to affect to the magnetic or expansion results discussed in this paper.²⁰ The refined lattice parameters and unit cell volumes determined from Rietveld analysis of the XRD data are listed in Table 2.1 and are consistent with those found in the open literature for LaFeO₃.^{1,}

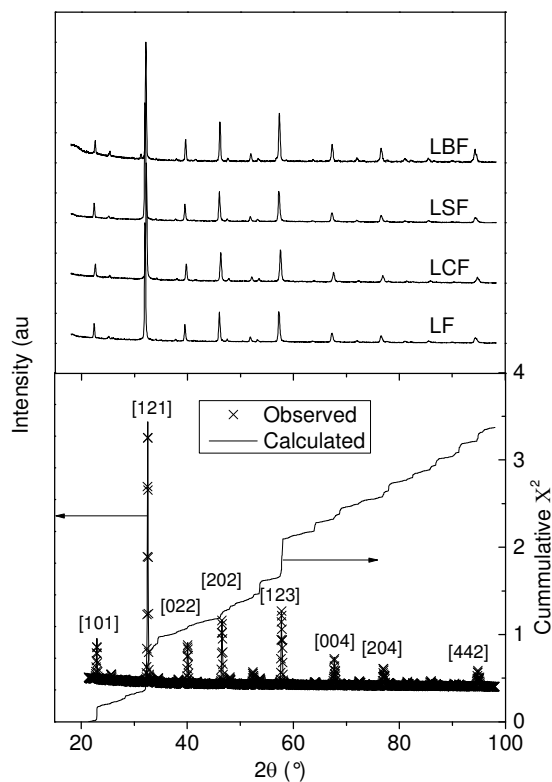


Fig. 2.1. XRD patterns at room temperature for all samples. Patterns are normalized and offset for comparison. Rietveld refinement for LF sample is shown in lower box with cumulative χ^2 and peak indexing.

Table 2.1. Lattice parameters and volume of each sample determined from XRD and the cell volume determined by the Ubic²² model.

	a (Å)	b (Å)	c (Å)	V (Å ³)	V _{calculated} (Å ³)
LF	5.5679±0.0002	5.5602±0.0002	7.8550±0.0003	243.1758±0.0140	241.365±0.780
LCF	5.5497±0.0005	5.5350±0.0006	7.8195±0.0008	240.1951±0.0435	238.8098±0.595
LSF	5.5555±0.0003	5.5337±0.0003	7.8584±0.0004	241.5890±0.0224	240.2796±0.563
LBF	5.5557±0.0004	5.556±90.0003	7.8540±0.0005	242.4716±0.0262	241.3618±0.465

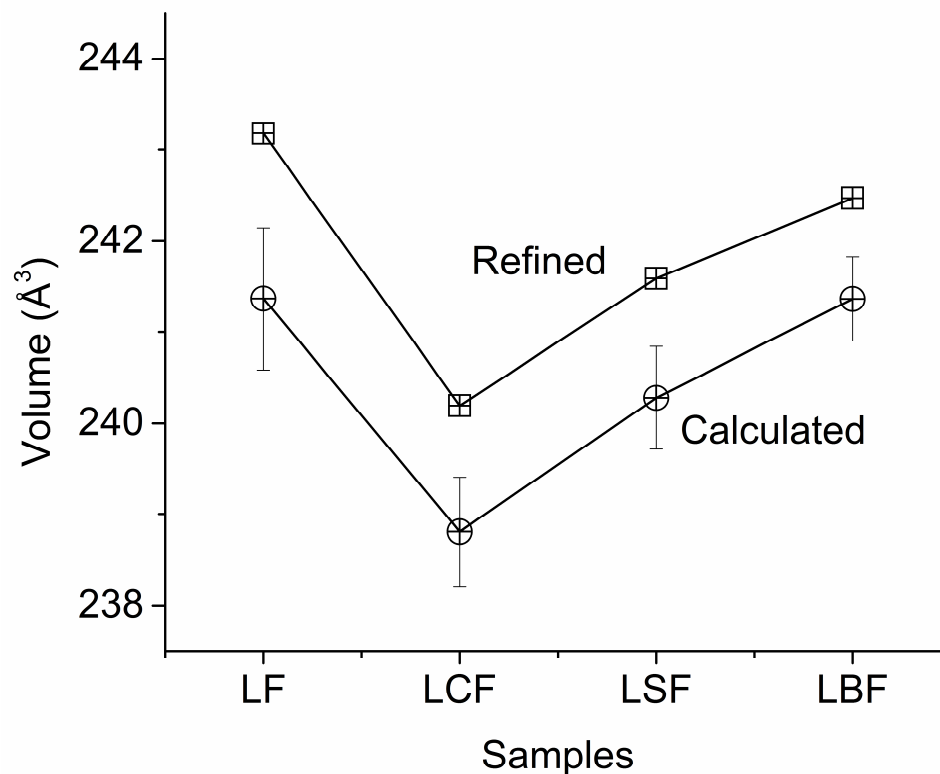


Fig. 2.2. Cell volume of samples as determined by Reitveld refined parameters and calculated using Ubic²² model.

The estimated Shannon ionic radii are dependent on the coordination, valence, and spin of each cation. In LaFeO_3 , the A site of the perovskite structure is coordinated with 12 oxygen sites, giving the ionic radii: $\text{La}^{3+}=1.50$, $\text{Ca}^{2+}=1.48$, $\text{Sr}^{2+}=1.58$, and $\text{Ba}^{2+}=1.75$ Å.²¹ Intuitively, the larger ionic radii of Sr and Ba would be expected to result in an increase in lattice parameters; however, the introduction of divalent cations caused a decrease in the calculated lattice parameters for all samples. This behavior can be explained if charge compensation is dominated by the conversion of Fe^{3+} to Fe^{4+} . The formation of tetravalent iron would cause a reduction in lattice parameters due to the smaller ionic radius of Fe^{4+} (0.785 Å) as compared to Fe^{3+} (0.725 Å).²¹ Ubic *et al.*²² proposed a model for estimating unit cell parameters. Ubic's model was used as a comparison for observed parameters and cell volumes calculated from both are shown in

Fig. 2.2. The calculated parameters were determined with full occupancy and only considered a charge compensation of Fe^{3+} to Fe^{4+} . The values determined were found to be consistently lower than the values determined from XRD. The difference could be explained by an error in the refinement or missing factors in the model (the model was based off of non-doped samples and may not consider variations due to substituted ions).

The high-temperature XRD data showed that the volume expansion about the Néel temperature, shown in Fig. 2.3, is continuous, implying that the transition is of second order. For temperatures lower than $T/T_N < 0.5$, the volume expansion was observed to be linear, and is projected in Fig. 2.3 to higher temperatures as indicated by the dashed line. Above $T/T_N > 0.5$, the rate of change in the volume expansion increases until $T/T_N = 1$, after which it decreases and is approximately equal to that observed at lower temperatures. This non-linear expansion behavior has been observed in other studies of the magnetoelastic effects on thermal expansion of lanthanum ferrite.^{4,9}

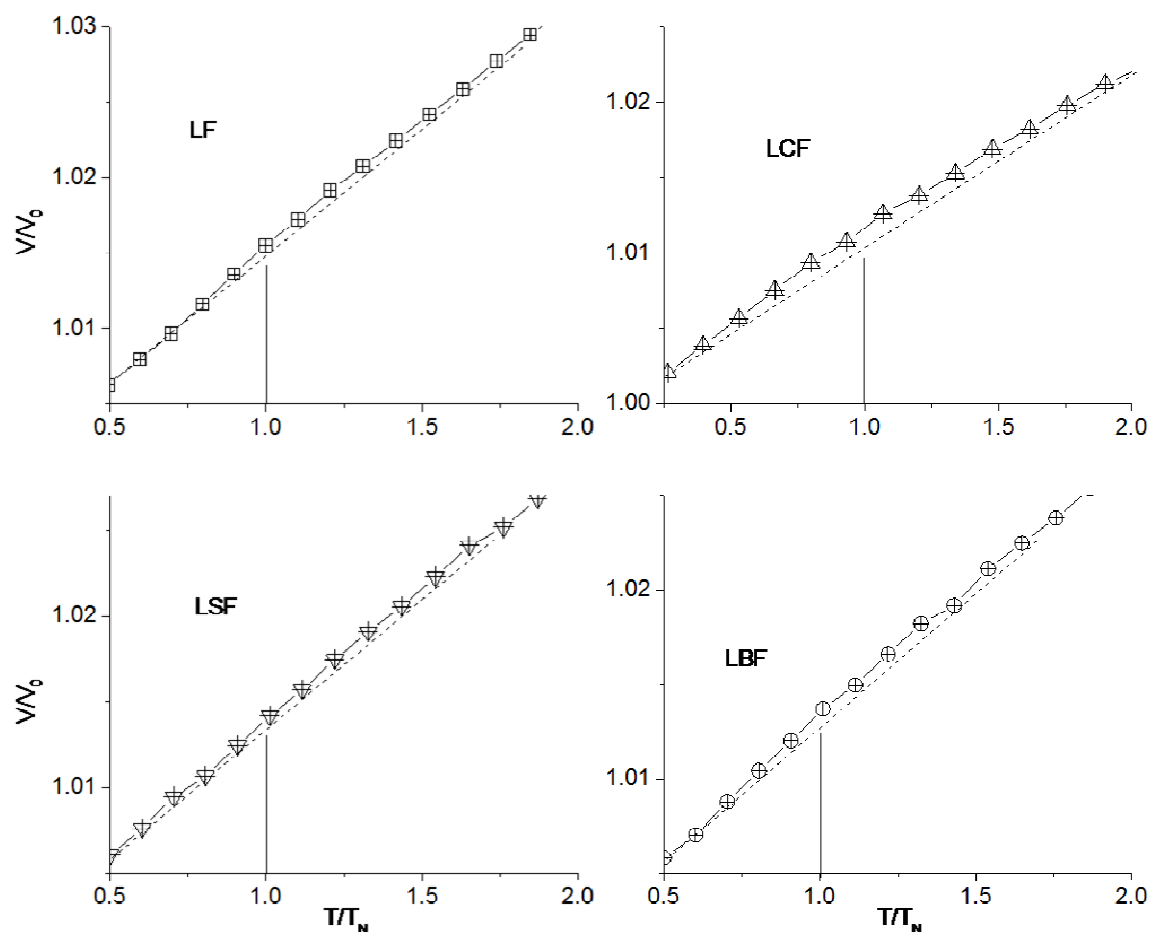


Fig. 2.3. The volume expansion measured by XRD about T_N . The linear, dashed line helps to illustrate the departures from linearity.

The changes in individual lattice parameters as a function of temperature are shown in Fig. 2.4 where shifts in the linearity, or changes in the thermal expansion coefficients, near T_N can be seen. In the case of LF and LSF, there were small but measurable shifts of all three lattice parameters occurring just prior to T_N . The LCF samples showed a significant shift in the rate of change in b and subtle shifts in the changes in a and c . No noticeable change in the expansion of LBF could be detected from these data, but in all three doped materials, i.e., LCF, LSF, and LBF, it is apparent

that the coefficient of expansion along the b direction (i.e., db/dT) is smaller at temperatures above T_N .

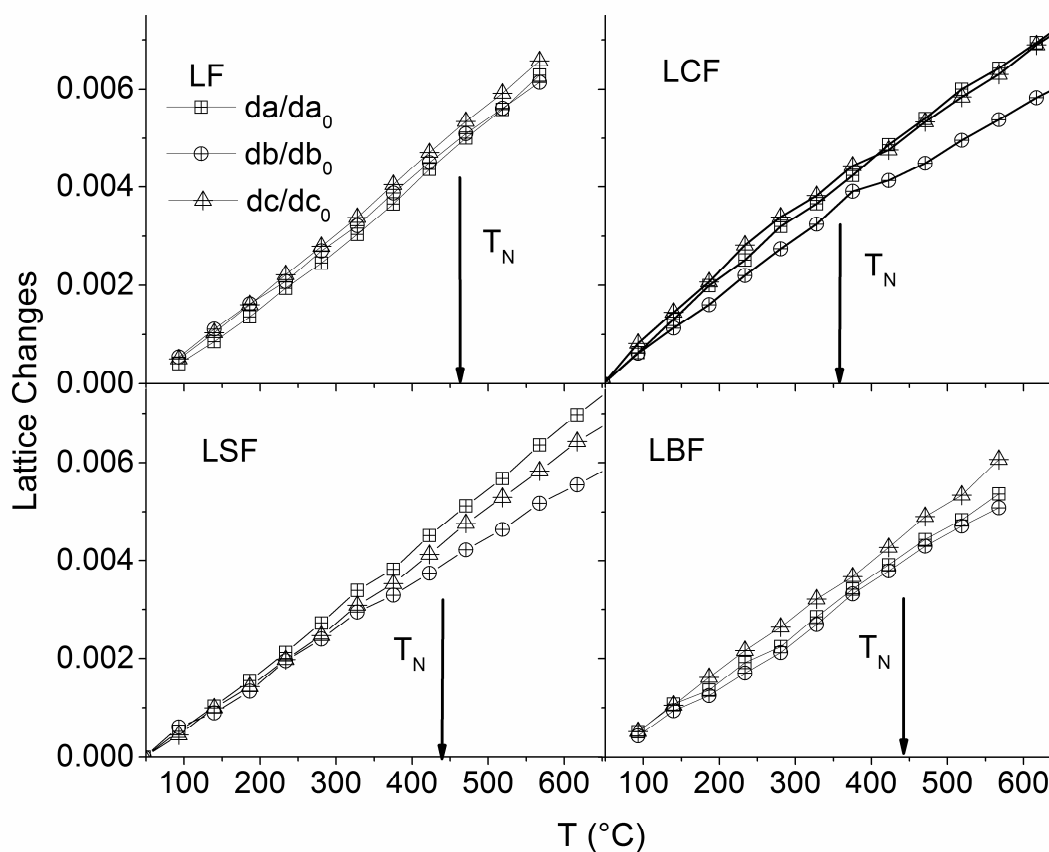


Fig. 2.4. Changes in lattice parameters, a, b, and c measured as a function of temperature by HT-XRD. The Néel temperatures are annotated by the drop lines for each sample: LF (upper left), LCF (upper right), LSF (lower left), and LBF (lower right).

2.3.2 Dilatometry

Dilatometry was used to find the instantaneous coefficients of thermal expansion (CTE) and apparent values of T_N (vertical lines) as shown in Fig. 2.5. The T_N values

measured by dilatometry for LF, LCF, LSF, and LBF are 457°C, 341°C, 440°C, and 442°C respectively and are consistently those found in the literature for LF, LCF, and LSF. The T_N for LBF has not been previously reported in the literature. A summary of the Néel temperatures measured by both dilatometry and magnetometry are compared with those reported in the literature in Table 2.2.^{4, 17} In all four samples, the CTE values increased approximately linearly as the temperature approached the respective T_N after which the values decreased or plateaued. The CTE behavior observed by dilatometry is consistent with the data obtained by high temperature XRD, where the volume expansion was non-linear about T_N . The dilatometry data in Fig. 2.4 indicates that the CTE of lanthanum ferrite increases linearly at a rate of 0.0102T for $T < T_N$, reaches a local maximum near T_N , and decreases linearly at a rate of 0.0055T for $T > T_N$. The data in Fig. 5 also show that three the divalent-doped materials behave similarly, reaching a local maximum in CTE near T_N . The non-linear volume expansion behavior and variations in the instantaneous CTE around T_N shown in Fig. 2.5 are consistent with expansion behavior around T_N found in LaFeO_3 by Selbach *et al.*⁹ These results illustrate that the magnetoelastic contribution or coupling (mechanism) to the thermal expansion found in LaFeO_3 is also present in divalent-cation substituted lanthanum ferrites.

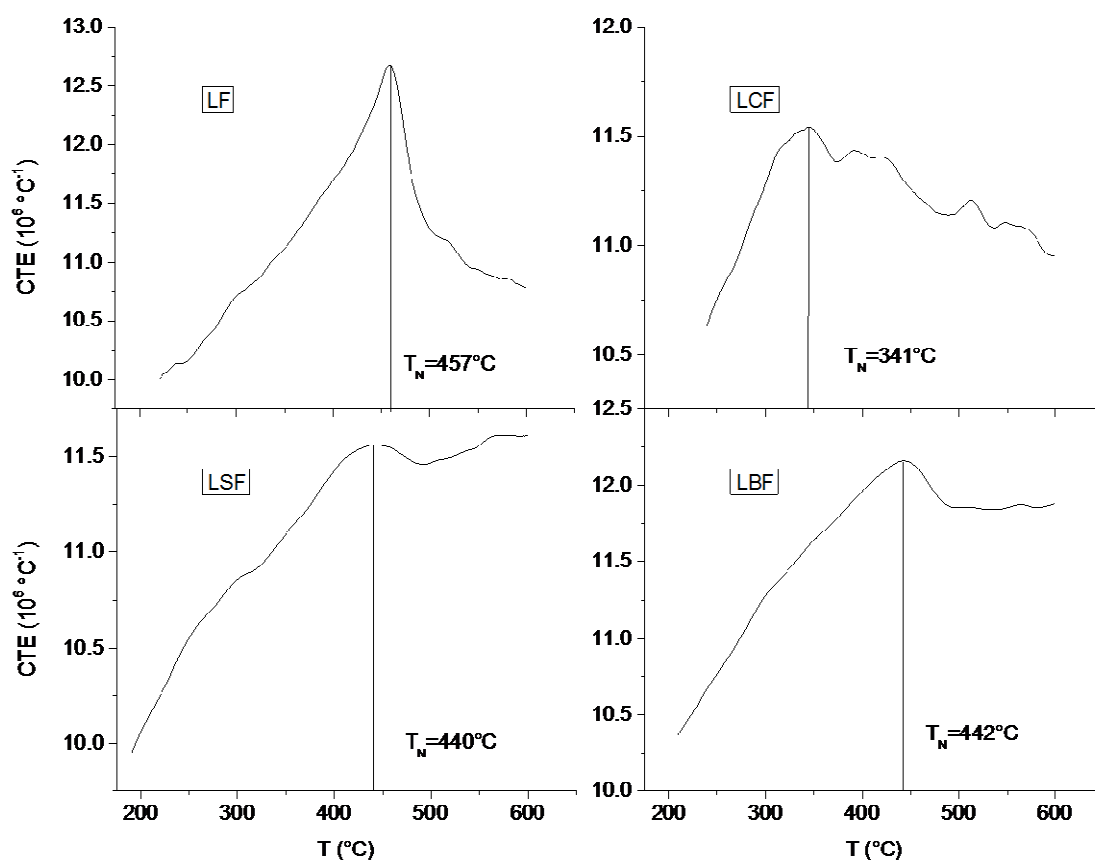


Fig. 2.5. Coefficients of thermal expansion measured by dilatometry. The changes in the linearity of the CTE indicate the Néel temperatures, as annotated by the drop lines.

Table 2.2. Comparisons of the Néel temperatures found for all samples observed in this study and T_N listed in literature. Komornicki and Wattiaux used Thermogravimetric Analysis to determine the Néel Temperature while Fossdal used HT-XRD.^{4, 15, 16}

Composition	T_N ($^\circ\text{C}$) from Dilatometry	T_N ($^\circ\text{C}$) from VSM	Komornicki ¹⁵	Fossdal ⁴	Wattiaux ¹⁶
LaFeO_3	457	471	477 $^\circ\text{C}$	450 $^\circ\text{C}$	452 $^\circ\text{C}$
$\text{La}_{0.9}\text{Ca}_{0.1}\text{FeO}_3$	341	351	-	-	-
$\text{La}_{0.9}\text{Sr}_{0.1}\text{FeO}_3$	440	465	-	380 $^\circ\text{C}$	$\approx 400^\circ\text{C}$
$\text{La}_{0.9}\text{Ba}_{0.1}\text{FeO}_3$	442	466	-	-	-
$\text{La}_{0.9}\text{Ca}_{0.2}\text{FeO}_3$	-	-	277 $^\circ\text{C}$	-	-

2.3.3 Vibrating Sample Magnetometry

Magnetization measurements were made by VSM as a function of temperature in order to directly determine the Néel temperature as shown in Fig. 2.6. The T_N values are indicated by relatively sharp peaks shown in Fig. 2.6. The T_N of LaFeO_3 was 471°C . The LSF and LBF samples had slightly lower values of T_N , 465°C and 466°C , respectively, and the T_N of LCF was the most suppressed at 351°C . Above T_N , the magnetization of LF remained relatively constant until approximately 520°C was reached and then decreased more rapidly with increasing temperature as the material became fully paramagnetic. In the cases of the doped samples, the magnetization decreases relatively rapidly at temperatures above T_N . The T_N values measured by magnetometry are consistent with the transition temperatures determined by dilatometry and further validate the conclusion that magnetostatic coupling is the mechanism of magnetic contribution to thermal expansion.

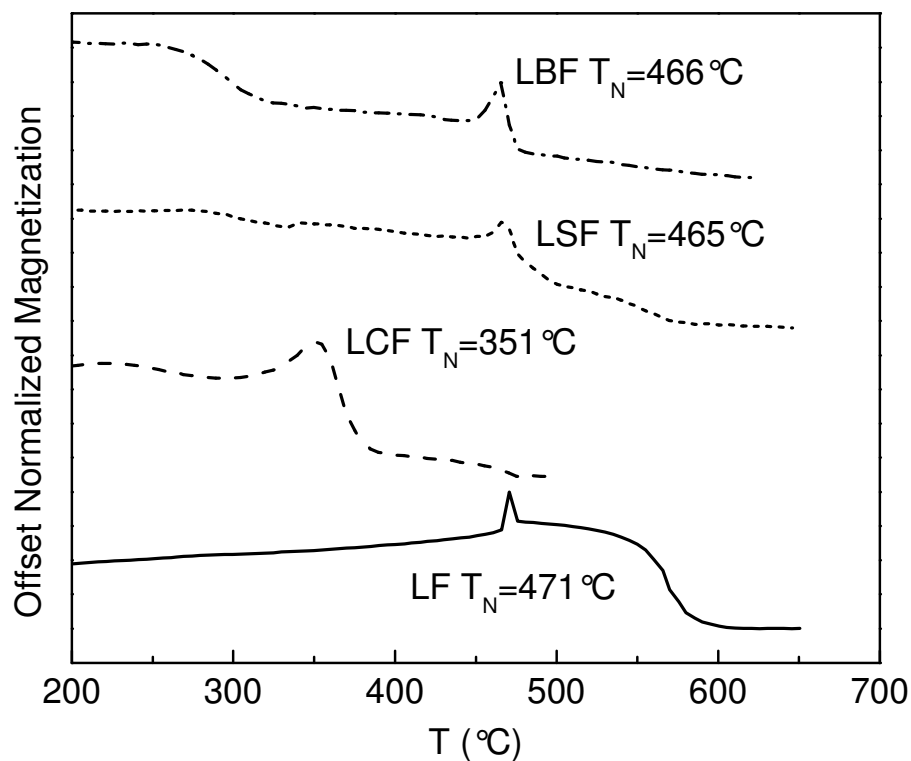


Fig. 2.6. Magnetometry results showing the Néel temperature (peaks) associated with the anti-ferromagnetic to paramagnetic transformations. The magnetizations are offset and normalized to better illustrate the relative changes in T_N .

The suite of characterization methods used in this study demonstrated that Ca substitutions result in a larger decrease in the Néel temperature compared to Sr or Ba substitutions where only very small changes in T_N were observed. If the reduction in Néel temperature was solely due to charge compensation by the formation of tetravalent iron, then all three of the divalent-doped lanthanum ferrite materials studied here would be expected to have approximately the same Néel temperature, therefore, the differences in the observed values of T_N must be associated at least in part by another competing mechanism. As stated earlier, divalent substitutions on the trivalent A site require charge compensation by either the creation of oxygen vacancies or the oxidation of Fe^{3+} ($3d^5$) to

Fe^{4+} ($3d^4$). In the event that Fe^{3+} changes to Fe^{4+} , the number of unpaired electrons available for magnetic coupling across the Fe-O-Fe bond (i.e., super-exchange) is reduced. Additionally, the coupling of Fe^{3+} -O- Fe^{4+} is weakly ferromagnetic and will reduce the Néel temperature as it breaks up the long range AFM ordering and causes an increase in the paramagnetic behavior of the material. The reduction in the Néel temperature of LCF observed in our materials was consistent with the experimental results of Komornicki *et al.*¹⁵ in which oxidized LCF samples, which were charge-compensated almost entirely by the formation of Fe^{4+} , showed a significant reduction in T_N (Table 2.2). Alternatively, Grenier *et al.*²³ found that the Néel temperature remained nearly constant regardless of the amount of divalent calcium substitution in LCF materials annealed in a low oxygen partial pressure environment. Grenier showed that there was no evidence of Fe^{4+} using Mössbauer spectroscopy, indicating that the charge compensation was exclusively associated with the formation of oxygen vacancies. Therefore, the AFM Fe^{3+} -O- Fe^{3+} coupling remained unaffected in samples populated by only Fe^{3+} because magnetic nearest neighbors remain unchanged throughout all of his compositions. The contrasting work of Komornicki *et al.*¹⁵ and Grenier *et al.*²⁰ clearly show that the extent of the suppression of the Néel temperature is dependent on the charge compensating mechanisms (Fe^{4+}/V_O ratio), which is dependent on both the concentration of divalent substitution and the partial pressure of oxygen to which the materials are exposed.

2.3.4 Neutron Diffraction

In addition to charge compensation mechanisms, structural distortions can also affect the Néel temperature. A correlation between AFM, T_N , and the Fe-O-Fe bond

angle has been investigated by several authors for RFeO₃ compounds.^{24, 25} These authors have suggested that as the Fe-O-Fe bond angle is increased along the direction of the super-exchange interaction, there is more overlap between the iron e_g (high energy d-orbital) and the oxygen 2p orbitals, resulting in an increase AFM strength and higher T_N. Zhou and Goodenough²⁶ showed a linear correlation between T_N and cos⁴($\omega/2$)/d⁷, where $\omega = (180-\theta)$, θ is the distortion angle, and d is the Fe-O bond length. This relationship can be used to estimate the difference between the expected T_N for calcium-, strontium-, or barium- substituted samples through linear extrapolation of data from Zhou and Goodenough. The neutron diffraction data in Table 2.3 indicates that the Fe-O1-Fe bond angle is increased from 156.8° in LaFeO₃ to 161.3° in LSF and 161.4° in LBF, and is reduced to 156.0° in LCF (the bond angle of interest is determined by the Fe and O1 atomic positions along the *Pbnm* c-axis). A simple calculation based on the differences of observed bond angles gives an estimated increase in T_N of about 50°C for LSF and LBF as compared to LCF.

Table 2.3. Fe-O1-Fe bond angle, change in T_N from bond angle changes, and moment/ion found through neutron diffraction. The moments are refined along the a-axis and the super exchange of Fe³⁺-O-Fe³⁺ occurs along the c-axis and corresponds to the Fe-O1-Fe bond angle. The ΔT_N listed is based on the assumption of identical iron content between samples and is determined solely upon the change in the Fe-O1-Fe bond angle.

	Bond Angles (°)	ΔT_N from Bond Angle	(μ_B /Fe)
LaFeO ₃	156.8	NA	3.77
La _{0.9} Ca _{0.1} FeO ₃	156	0	3.15
La _{0.9} Sr _{0.1} FeO ₃	161.3	+50	2.8
La _{0.9} Ba _{0.1} FeO ₃	161.4	+50	3.08

The Néel temperature of oxidized, Ca-substituted samples is greatly reduced because of the nearly complete charge compensation through the formation of tetravalent iron, rather than oxygen vacancies, and a slight decrease in the Fe-O1-Fe bond angle. The Sr- and Ba-doped samples also have a suppressed T_N due to the formation of Fe^{4+} but also have increased Fe-O1-Fe bond angles, which increases the magnetic coupling and thus increases the strength of the super-exchange interactions between the remaining Fe^{3+} pairs. The estimated increase in T_N (50°C) due to the increase in bond angle is not sufficient to explain the large difference in T_N ($\Delta \approx 100^\circ\text{C}$) between LCF and the LSF and LBF samples. Consequently, it is likely that partial charge compensation by vacancies is more prevalent in the LSF and LBF systems than in the LCF system. Further assessment on the charge compensation mechanism has been reported by Price *et al.*²⁷

It is notable that only the Fe-O1-Fe bond angle increased with divalent cation substitutions, while the Fe-O2-Fe bond angle remained nearly constant, as shown in Table 2.3. The ideal cubic perovskite unit cell contains three equivalent oxygen lattice sites. In non-cubic perovskites, octahedral tilting reduces the symmetry and the unit cell expands accordingly. In the case of the *Pbnm* orthorhombic structure, the reduction of symmetry creates two unique oxygen lattice sites (O1 and O2). There are twice the number of O2 lattice sites (8) as there are O1 lattice sites (4). The O1 oxygen atoms are located at the vertices of the FeO_6 octahedra and align along the long *c*-axis of the *Pbnm* unit cell, as shown in Fig. 2.7.

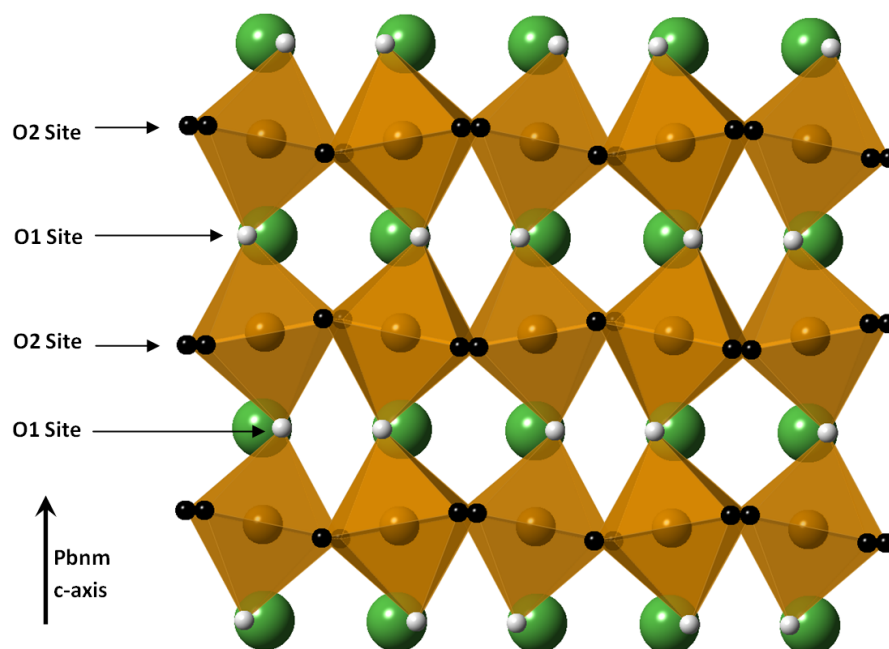


Fig. 2.7. The *Pbnm* structure of LaFeO_3 . The O1 site oxygen atoms shown in white are located at the vertices of the FeO_6 octahedra and are aligned along the long *c*-axis. The large A site cations are shown in green. The iron cations are shown in the center of the octahedra.

Huspeh *et al.*²⁸ deduced, from neutron diffraction data, that the direction of the AFM moment is indiscernible between the two nearly equivalent pseudo-cubic lattice parameters, as was the case in our neutron diffraction data.²⁷ However, the correlation between the Néel temperature and the calculated Fe-O1-Fe bond angle suggests that the super-exchange interaction occurs along the long axis. This correlation is further strengthened by the fact that super-exchange is maintained along the symmetrically similar long axes of the lanthanum ferrite perovskite derivatives, known as the Grenier and brownmillerite structures. These results are consistent with high-resolution neutron-diffraction data of LaFeO_3 shown by Peterlinneumaier and Steichele,²⁹ which indicate that the direction of AFM is slightly canted along the *a*-axis of the *Pbnm* unit cell. It is

suspected that the direction of the canted AFM behavior is preserved along the a-axis in the divalent cation-substituted lanthanum ferrite materials studied here.

2.4 Conclusions

The thermal expansion behaviors of pure LaFeO_3 and $\text{La}_{0.9}\text{R}_{0.1}\text{FeO}_3$ (R=Ca, Sr, Ba) were correlated with the anti-ferromagnetic-to-paramagnetic phase transformations using a combination of dilatometry, vibrating sample magnetometry, and high temperature x-ray diffraction. Néel temperatures determined via dilatometry, XRD, and VSM were in agreement and were consistent with values available in literature. This is the first such study that has used a combination of these three techniques to measure both the Néel temperature and expansion behavior for alkaline-doped perovskites. The results confirm those of Selbach *et al.*⁹ who suggested that the thermal expansion behavior has contributions from magneto-static coupling.

Differences between the observed Néel temperatures in LF, LCF, LSF, and LBF specimens were attributed to both the nature of the charge compensation mechanism and the effect of the substituent on the super-exchange bond angle. For divalent calcium-substituted LaFeO_3 , the Néel temperature is significantly reduced due to the reduction of Fe^{3+} to Fe^{4+} from charge compensation and a decreased Fe-O1-Fe bond angle. For strontium- and barium-substituted LaFeO_3 , it is suspected that charge compensation was accomplished by both the reduction of iron from Fe^{3+} to Fe^{4+} and the formation of oxygen vacancies. Due to the formation of oxygen vacancies in Sr and Ba substituted samples, the number of iron ions being reduced to Fe^{4+} decreases compared to the Ca doped samples and the disruption to the long range magnetic ordering is low. In addition, the disruption to long range magnetic ordering is mitigated by an increase in the Fe-O1-Fe

bond angle and the super exchange interaction is strengthened. These two factors, oxygen vacancy formation and increased bond angle, cause the strontium and barium doped samples to have only a minor decrease in Néel temperature. The correlation between calculated bond angles from neutron diffraction data and Néel temperatures suggest that the super-exchange still occurs along the *c*-axis of the *Pbnm* unit cell for divalent doped samples. The directions of the anti-ferromagnetic moment in LCF, LSF, and LBF were indiscernable from our data, but likely remained slightly canted along the *a*-axis, as is suggested in literature for the case of pure LF.

2.5 Acknowledgements

This research was partially supported by the NRC-38-08-955 nuclear materials fellowship.

2.6 Author Justifications

The research presented in this publication was authored by Geoffrey L. Beausoleil II as partial fulfillment of the requirements for a Master of Science degree in Materials Science and Engineering at Boise State University. Research carried out in this publication was carried out by Patrick Price and David Thompsen. Scott Misture and Alfred University were especially gracious in making their XRD facilities available to us. Sven Vogel at Los Alamos was of great help in assisting in the neutron diffraction study mentioned in this paper and Patrick Price's work on it (a small portion of a much larger study) was invaluable. In addition, Dr. Darryl Butt, Dr. Alex Punnoose, and Dr. Rick Ubic made significant contributions toward this work in terms of providing the necessary guidance, materials, equipment, and funding for the success of the experiments presented.

2.7 References

1. S. Acharya, J. Mondal, S. Ghosh, S. K. Roy, and P. K. Chakrabarti, "Multiferroic Behavior of Lanthanum Orthoferrite (LaFeO_3)," *Mater. Lett.*, **64** [3] 415-18 (2010).
2. P. N. Dyer, M. F. Carolan, D. P. Butt, R. M. P. H. van Doorn, R. A. Cutler, and K. D. Gourley, "Mixed Conducting Membranes for Syngas Production," Australia Patent #2001295502. 2005.
3. M. F. Carolan, P. N. Dyer, R. M. P. H. van Doorn, R. A. Cutler, and D. P. Butt, "Ion Transport Membranes for Syngas Production," U.S. Patent #6492290. 2003.
4. A. Fossdal, M. Menon, I. Waernhus, K. Wiik, M. A. Einarsrud, and T. Grande, "Crystal Structure and Thermal Expansion of $\text{La}_{1-x}\text{Sr}_x\text{FeO}_{3-\delta}$," *J. Am. Ceram. Soc.*, **87** [10] 1952-58 (2004).
5. L. C. Bartel, "Calculation of Near Neighbor Spin Correlation Functions in MNO and α -MNS for T Less Than T_N ," *Bull. Am. Phys. Soc.*, **15** [3] 271 (1970).
6. L. C. Bartel, "Magnetic Contribution to Thermal Expansion in an Itinerant Antiferromagnet," *J. App. Phys.*, **41** [13] 5132 (1970).
7. M. E. Lines and E. D. Jones, "Antiferromagnetism in Face-Centered Cubic Lattice α -Mns," *Phys. Rev.*, **141** [2] 525 (1966).
8. R. E. Taylor, "Thermal Expansion of Solids." ASM International: Materials Park, OH, (1996).
9. S. M. Selbach, J. R. Tolchard, A. Fossdal, and T. Grande, "Non-linear Thermal Evolution of the Crystal Structure and Phase Transitions of LaFeO_3 Investigated by High-temperature X-ray Diffraction," *J. Solid State Chem.*, **196** 249-54 (2012).

10. I. Waernhus, P. E. Vullum, R. Holmestad, T. Grande, and K. Wiik, "Electronic Properties of Polycrystalline LaFeO_3 . Part I: Experimental Results and the Qualitative Role of Schottky Defects," *Solid State Ionics*, **176** [37-38] 2783-90 (2005).
11. I. Waernhus, T. Grande, and K. Wiik, "Electronic Properties of Polycrystalline LaFeO_3 . Part II: Defect Modelling Including Schottky Defects," *Solid State Ionics*, **176** [35-36] 2609-16 (2005).
12. M. Ghaffari, M. Shannon, H. Hui, O. K. Tan, and A. Irannejad, "Preparation, Surface State and Band Structure Studies of $\text{SrTi}_{1-x}\text{Fe}_x\text{O}_{3-\delta}$ ($x = 0-1$) Perovskite-Type Nano Structure by X-ray and Ultraviolet Photoelectron Spectroscopy," *Surf. Sci.*, **606** [5-6] 670-77 (2012).
13. M. Ghaffari, T. Liu, H. Huang, O. K. Tan, and M. Shannon, "Investigation of Local Structure Effect and X-ray Absorption Characteristics (EXAFS) of Fe (Ti) K-edge on Photocatalyst Properties of $\text{SrTi}_{1-x}\text{Fe}_x\text{O}_{3-\delta}$," *Mater. Chemistry and Physics*, **136** [2-3] 347-57 (2012).
14. V. N. Stathopoulos, V. C. Belessi, T. V. Bakas, S. G. Neophytides, C. N. Costa, P. J. Pomonis, and A. M. Efstathiou, "Comparative Study of La-Sr-Fe-O Perovskite-Type Oxides Prepared by Ceramic and Surfactant Methods Over the CH_4 and H_2 lean-de NO_x ," *Appl. Catal., B*, **93** [1-2] 1-11 (2009).
15. S. Komornicki, L. Fournes, J. C. Grenier, F. Menil, M. Pouchard, and P. Hagenmuller, "Investigation of Mixed Valency Ferrites $\text{La}_{1-x}\text{Ca}_x\text{FeO}_{3-\delta}$ ($0 \leq x \leq 0.50$) With the Perovskite Structure," *Mater. Res. Bull.*, **16** [8] 967-73 (1981).

16. A. Wattiaux, J. C. Grenier, M. Pouchard, and P. Hagenmuller, "Electrolytic Oxygen Evolution in Alkaline-Medium on $\text{La}_{1-x}\text{Sr}_x\text{FeO}_{3-\delta}$ Perovskite-Related Ferrites 2: Influence of Bulk Properties," *J. Electrochem. Soc.*, **134** [7] 1718-24 (1987).
17. M. A. Ahmed and S. I. El-Dek, "Extraordinary Role of Ca^{2+} ions on the Magnetization of LaFeO_3 Orthoferrite," *Mater. Sci. Eng., B*, **128** [1-3] 30-33 (2006).
18. B. H. Toby, "EXPGUI, a Graphical User Interface for GSAS," *J. Appl. Cryst.* **34** 210-13 (2001).
19. A. C. Larson, "General Structure Analysis System (GSAS)," pp. 86-748. in., Los Alamos National Laboratory, *LAUR* 1994.
20. P. Brovetto, A. Delunas, V. Maxia, D. Mazza, and M. Vallino, "Antiferromagnetism in Double-Layered Perovskitic Oxides $\text{SrLa}_2\text{Fe}_2\text{O}_7$ and $\text{BaLa}_2\text{Fe}_2\text{O}_7$," *Nuovo Cimento Della Societa Italiana Di Fisica D-Condensed Matter Atomic Molecular and Chemical Physics Fluids Plasmas Biophysics*, 13[11] 1425-28 (1991).
21. R. D. Shannon, "Revised Effective Ionic-Radii and Systematic Studies of Interatomic Distances in Halides and Chalcogenides," *Acta Crystallographica Section A*, 32[SEP1] 751-67 (1976).
22. R. Ubic, "Revised Method for the Prediction of Lattice Constants in Cubic and Pseudocubic Perovskites," *Journal of the American Ceramic Society*, 90[10] 3326-30 (2007).
23. J. C. Grenier, L. Fournes, M. Pouchard, and P. Hagenmuller, "Mossbauer Resonance Studies on the $\text{Ca}_2\text{Fe}_2\text{O}_5$ - LaFeO_3 System," *Materials Research Bulletin*, 17[1] 55-61 (1982).

24. Y. Nagata, S. Yashiro, T. Mitsuhashi, A. Koriyama, Y. Kawashima, and H. Samata, "Magnetic properties of $RFe_{1-x}Mn_xO_3$ ($R = Pr, Gd, Dy$)," *Journal of Magnetism and Magnetic Materials*, 237[3] 250-60 (2001).
25. I. S. Lyubutin, T. V. Dmitrieva, and A. S. Stepin, "Dependence of Exchange Interactions on Chemical Bond Angle in a Structural Series: Cubic Perovskite-Rhombic Orthoferrite-Rhombohedral Hematite," *Journal of Experimental and Theoretical Physics*, 88[3] 590-97 (1999).
26. J. S. Zhou and J. B. Goodenough, "Intrinsic Structural Distortion in Orthorhombic Perovskite Oxides," *Physical Review B*, 77[13] (2008).
27. P. Price, S. Radenberg, S. Misture, and D. P. Butt, "Phase Transformation in Lanthanum Calcium Orthoferrites." in., 2013.
28. J. M. Hudspeth, G. A. Stewart, A. J. Studer, and D. J. Goossens, "Crystal and Magnetic Structures in Perovskite-related $La_{1-x}Ca_xFeO_3$ ($x=0.2, 0.33$)," *Journal of Physics and Chemistry of Solids*, 72[12] 1543-47 (2011).
29. T. Peterlinneumaier and E. Steichele, "Antiferromagnetic Structure of $LaFeO_3$ From High-Resolution ToF Neutron-Diffraction," *Journal of Magnetism and Magnetic Materials*, 59[3-4] 351-56 (1986).

CHAPTER THREE: PHASE TRANSITIONS OF $\text{La}_{0.9}\text{Ca}_{0.1}\text{Fe}_y\text{O}_{3-\delta}$ AT LOW OXYGEN
PARTIAL PRESSURES

This chapter has been submitted for publication to Elsevier in *Journal of the American Ceramic Society* and should be referenced appropriately.

Reference:

G. L. Beausoleil II, Patrick Price, Alex Punnoose, Darryl P. Butt. *Phase Transformation of Reduced $\text{La}_{0.9}\text{Ca}_{0.1}\text{Fe}_y\text{O}_{3-\delta}$ ($y=1.000, 0.995, 0.990$)*. J. Amer. Cer. Soc., (submitted) 2013

*This chapter includes modifications from the originally submitted version.

Phase Transitions of $\text{La}_{0.9}\text{Ca}_{0.1}\text{Fe}_y\text{O}_{3-\delta}$ at Low Oxygen Partial Pressures

Geoffrey L. Beausoleil II¹

Patrick Price

Alex Punnoose²

Darryl P. Butt^{1,3,*}

Submitted for publication in:

Journal of Solid State Ionics

July 2013

¹Department of Materials Science & Engineering and ²Department of Physics, Boise
State University, Boise, ID 83725

³Center for Advanced Energy Studies, Idaho Falls, ID 83401

Abstract

The phase equilibria of calcium-doped lanthanum ferrite ($\text{La}_{0.9}\text{Ca}_{0.1}\text{Fe}_y\text{O}_{3-\delta}$) were assessed at temperatures to 1100°C in air, argon, and 5% $\text{H}_2\text{-N}_2$ as a function of Fe concentration ($y = 1.000, 0.995, 0.990$). Phase transformations were characterized using a combination of dilatometry, x-ray diffraction, electron microscopy, differential scanning calorimetry, differential thermal analysis, and thermogravimetric analysis. Two transformations were observed, a relatively low temperature ($345\text{-}468^\circ\text{C}$) magnetic phase transformation and a higher temperature ($835\text{-}883^\circ\text{C}$) orthorhombic to rhombohedral transformation. The samples made with nominal iron deficiencies behaved as if they had a decreased concentration of calcium. The magnetic or so called Néel transition temperature was found to increase with decreasing iron content and decreasing oxygen partial pressure, P_{O_2} . The transition temperature associated with the orthorhombic to rhombohedral transformation was also found to decrease with P_{O_2} but increased with decreasing iron content.

3.1 Introduction

Perovskites comprised of rare earth elements have been studied for many decades due to the variety of useful properties that they have and the ease of modifying or tailoring properties through processing and adjustments in composition. Perovskites have a pseudo-cubic structure of the form ABO_3 , such as CaTiO_3 , where the A- and B-sites are occupied with cations most often of valences 2+ and 4+, respectively. Typically, the A-site is a larger cation such as alkaline or rare earth metals and the B-site is often a smaller transition metal such as iron or titanium. The thermal and physical properties can be

manipulated by combining different cations on the A- or B-sites to form various defects such as oxygen vacancies or affecting the oxidation states of certain cations.

Lanthanum ferrite- (LaFeO_3) based perovskites have been shown to have mixed electronic-ionic conductivity, with possible applications in gas separation, catalysis, syngas production, fuel cells, and hybrid energy production[1-4]. The most common substitutions include 2+ alkaline metals on the La- or A-site and transition metals on the Fe- or B-site, which generally results in increased ionic conductivity as the valence differences can lead to the creation of both oxygen vacancies and enhanced electrical conductivity[5-7].

In the specific case of a calcium substitution in LaFeO_3 , it has been shown that the primary mechanism for charge compensation for low concentrations of calcium in oxidizing conditions, less than 20 mole percent, is the oxidation of Fe^{3+} to Fe^{4+} with a very small amount of oxygen vacancies formed[3, 5, 8, 9]. It has also been shown in Sr-doped LaFeO_3 that the preferential mechanism of charge compensation in the room temperature structure is the oxidation of iron to Fe^{4+} , but upon heating weakly bound oxygen is released and oxygen vacancies are formed[10]. It was suggested that the oxygen was released in an ordered fashion throughout the bulk of the material, causing a general elongation of the lattice parameters. The release of oxygen would also cause the Fe^{4+} to be reduced back to Fe^{3+} in order to maintain charge neutrality. In addition, Mori *et al.*[11] investigated the thermal expansion coefficients, α , of Ca- and Sr-doped lanthanum manganites and found that for Ca contents of $0 \leq x \leq 0.1$ changes in α were affected primarily by oxygen release and the increase of the average ionic radii of B-site cations as the valence is reduced from 4+ to 3+.

While numerous studies have been conducted to assess the impacts of oxygen vacancies and multiple transition metals on the B-site, there has been little study on the effects on non-stoichiometry on the B-site itself, and in particular B-site deficiencies. In this study, calcium is substituted on the A-site of lanthanum ferrite at a fixed nominal concentration of 10% with a varying amount of iron to create iron deficient samples. With the introduction of 10% calcium, a relatively low amount, charge compensation should be dominated by further oxidation of the iron from Fe^{3+} to Fe^{4+} with a negligible amount of oxygen vacancies formed. However, the synthesis of samples with a nominal iron deficiency will require either the formation of iron vacancies or will maintain a stoichiometric material by limiting the number of available A sites. If there is a limit to the number of A sites, then a random or preferential selection of A site species will occur.

3.2. Experimental Methods

3.2.1 Sample Preparation

Calcium-doped lanthanum ferrite ($\text{La}_{0.9}\text{Ca}_{0.1}\text{Fe}_y\text{O}_{3-\delta}$) was fabricated with three Fe concentrations ($y = 1.000, 0.995, 0.990$) using the solid state reaction method previously reported.¹² For the purpose of brevity, each variation of sample composition, $y = 1.000, 0.995, 0.990$, will be denoted as Fe00, Fe05, and Fe10, respectively. The phase purity of the starting samples was verified by x-ray diffraction (XRD) using a Bruker (5465 East Cheryl Parkway, Madison WI 53711, USA) AXS D8 x-ray diffractometer with parallel beam geometry and a Panalytical (117 Flanders Road, Westborough MA 01581, USA) X'Pert x-ray diffractometer. XRD was done at room temperature with Cu K_α x-rays of wavelength 1.5418 Å. Diffraction data from XRD and were analyzed using the Rietveld

method and the General Structure Analysis System (GSAS) code with the EXPGUI graphical user interface.^{13, 14}

Following initial characterization, the powders were mixed with 30% by mass crystalline cellulose, pressed into pellets, and annealed in air at 1100°C to create porous pellets. Some of the pellets were set aside for dilatometry and TGA-DSC/DTA analysis and the others were treated under varying atmospheric conditions in a Thermolyne 59300 high-temperature tube furnace (81 Wyman Street, Waltham Ma 02454, USA).

3.2.2 Characterization Methods

In all controlled-atmosphere experiments, including annealing, dilatometry, thermal gravimetric analysis (TGA), differential scanning calorimetry (DSC), and differential thermal analysis (DTA), the samples were exposed to slightly pressurized, certified dry air (20% O₂-N₂), ultra high purity Ar (UHP-Ar), or UHP 5% H₂-N₂. In order to verify the oxygen partial pressure an Ametek (1100 Cassatt Rd., Berwyn, PA 19312, USA) CG1100 oxygen analyzer was used for the UHP-Ar and an Ametek 303B moisture analyzer was used for the 5% H₂-N₂. The temperature was ramped at 10°/min from room temperature to 1100°C for all experiments except the dilatometry in 5% H₂-N₂, which was limited to 900°C. The experiments run in air and Ar were held at temperature for one hour, at which point mass loss or gain plateaued and no further oxidation or reduction occurred. For the experiments run in 5% H₂-N₂, samples were held at temperature for 4 hours to allow for mass loss or gain to plateau.

Thermogravimetric and calorimetric data were collected on a Netzsch (129 Middlesex Turnpike, Burlington, MA 01803) 449 F3 Jupiter Simultaneous TGA-DSC/DTA. Experiments run in air and UHP-Ar used Pt crucibles with a DSC sample

carrier and for experiments run in 5% H₂-N₂ a tungsten crucible and a DTA sample carrier was used. Dilatometry was performed on a Netzsch Dil 402 E dilatometer using ~12 x 2 x 2 mm rods and held in an alumina sample carrier. Dilatometry experiments were corrected using a 12 mm Al₂O₃ polycrystalline standard.

Scanning electron microscopy (SEM) and energy dispersive spectroscopy (EDS) were performed using a Hitachi (Europark Fichtenhain A12, 47807 Krefeld, Germany) S-3400N VP-SEM with an Oxford Instruments (300 Baker Avenue, Concord, MA 01742, USA) Energy+ electron dispersive spectrometer. X-ray photoelectron spectroscopy was performed using a PHI (18725 Lake Drive East, Chanhassen, MN 55317) VersaProbe II Scanning XPS Microprobe with an Al x-ray source.

3.3 Results and Discussion

3.3.1 X-Ray Diffraction

Lanthanum ferrite samples with 10% calcium substitution and nominal B site deficiency (La_{0.9}Ca_{0.1}Fe_yO_{3-δ}) were successfully fabricated and were shown to be phase pure by x-ray diffraction and SEM. All compositions were confirmed by XRD to be orthorhombic with *Pnma* symmetry, regardless of the starting iron content, as shown in Fig. 3.1, which presents the patterns and Rietveld analyses of the baseline materials. The samples were further characterized using EDS and SEM to assure that there were no minor second phases or segregation in the starting material. The grain sizes of each material were verified to be 1-2 μm using SEM and backscattered electron imaging. Chemical compositions were measured for as-prepared samples using EDS and XPS and are shown in Fig. 3.2. The iron content determined from both methods was near constant

and does not give any indication as to the formation of B site vacancies during preparation. In addition, the La/Ca ratio has some variation between samples but no clear pattern suggesting whether one species is favored over another.

Previous research on B site deficient perovskites showed the formation of a secondary phase called the Ruddlesden-Popper phases (RP).¹⁵⁻¹⁷ Beznosikov *et al.*¹⁸ established geometric limits on the size of cations for RP phase where $R_A \leq 0.73R_X$. Therefore, due to these geometric limitations, the RP phase can be ruled out as a possible phase in either sample.

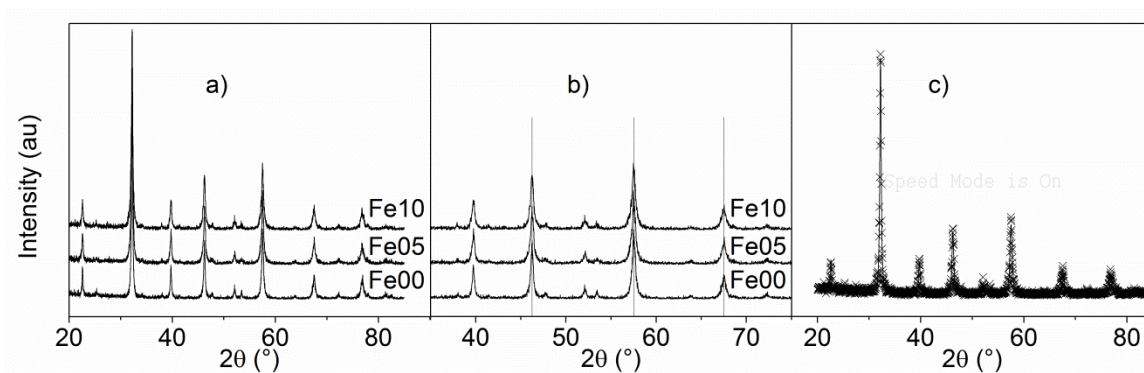


Fig 3.1. a) Full XRD patterns of as-prepared samples and b) the high-angle patterns to highlight the peak positions. B) Rietveld refinement calculated line and observed points to show an example of the refinements done.

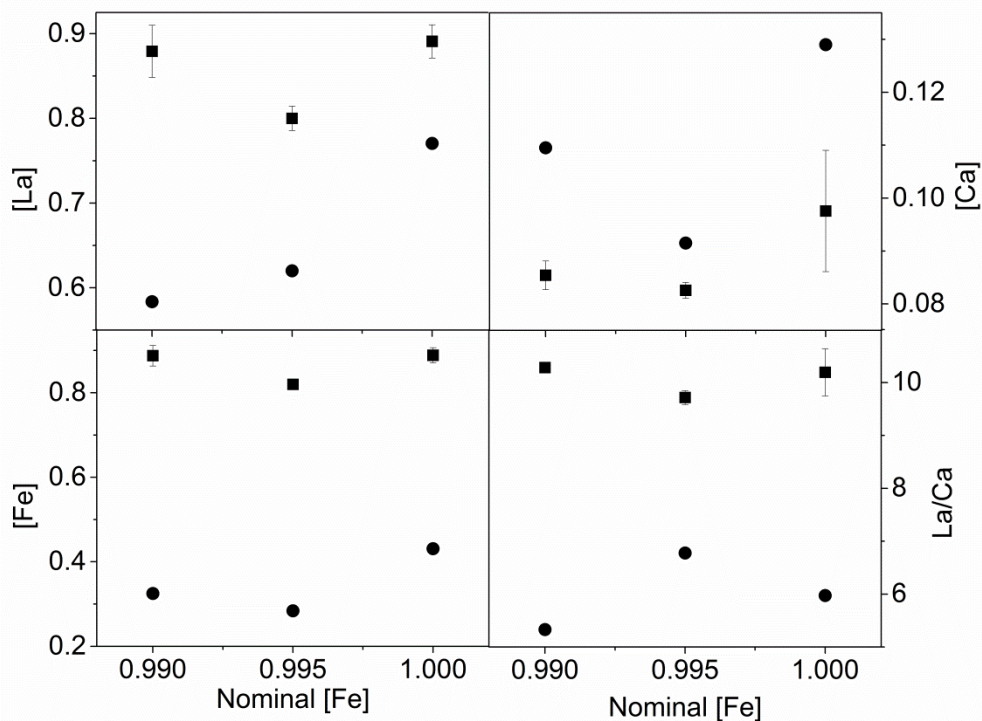


Fig 3.2. Concentrations of La, Ca, Fe and La/Ca ratio of as-prepared samples determined by EDS (solid squares) and XPS (solid circles). EDS points were determined by the mean of 20+ scans with a 95% confidence.

As shown in Fig. 3.1, the iron deficiency created little discernable difference in the XRD peak position nor, as shown in Fig. 3.3, were there measurable differences between the calculated lattice parameters ($<0.01\text{\AA}$). It has been suggested in previous studies the unit cell contracts with the introduction of calcium due to the decreased ionic radii of Fe^{4+} ($r_i = 0.725\text{\AA}$) compared to Fe^{3+} ($r_i = 0.785\text{\AA}$).^{3, 5, 9, 19} However, the contraction of the cell from calcium doping may be disrupted by making the samples iron deficient. In a study on B site deficiencies, Mori *et al.*²⁰ investigated the impacts of both A site and B site non-stoichiometry on La-doped SrTiO_3 and found that the cell expands with the introduction of Ti vacancies. They suggested that this is due to an increase in Coulombic repulsion between the oxygen anions and the large negative charge of the Ti

vacancy. This would also be expected in FE05 and Fe10 but there is a negligible change in the lattice parameters or cell volume. If iron vacancies are not forming, then there should be a change in composition of La, Ca, or both.

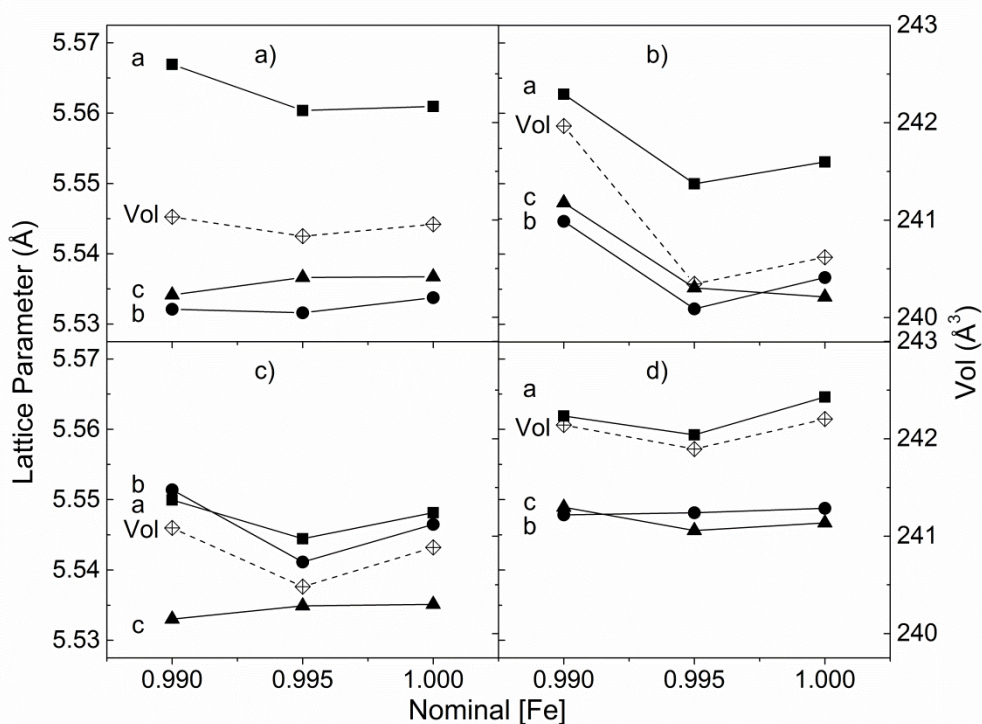


Fig. 3.3. Lattice parameters and cell volume of all samples determined from Rietveld refinement. The b parameter is described by the ratio $b_{\text{shown}} = b_{\text{actual}} / \sqrt{2}$.

Figure 4 shows the XRD patterns of the thermally treated samples. In the high angle patterns, drop lines are annotated on the position of the Fe00 peaks to show there is a shift to lower 2θ values as the nominal iron content is decreased. This shift in peak position is consistent with studies on varying concentrations of alkaline doping where lattice parameters decrease with increasing alkaline concentration.^{3, 5, 9} The peak shift to a lower 2θ suggests that the nominally iron-deficient samples are forming stoichiometric

samples and rejecting the calcium to maintain charge neutrality, thus forming samples with an effective composition of $\text{La}_{0.9+x}\text{Ca}_{0.1-x}\text{FeO}_3$. However, with only a small amount of iron vacancy formation, there could also be relaxation in the octohedra and thus a decrease in d-spacing and a shift to a lower 2θ . The only compensation mechanisms that can be ruled out from the peak position shift are the preferential selection of calcium over lanthanum and random selection of either lanthanum or calcium.

In a study by Dann *et al.*⁸ on Sr-doping of LaFeO_3 under oxidizing and reducing conditions, $0 \leq [\text{Sr}] \leq 0.2$, it was shown that all compositions maintained *Pnma* symmetry regardless of the atmosphere but there was a decrease in the orthorhombic distortion after exposure to 5% $\text{H}_2\text{-N}_2$. Our findings were in agreement with Dann's where each of the three $\text{La}_{0.9}\text{Ca}_{0.1}\text{Fe}_y\text{O}_{3-\delta}$ compositions retained their *Pnma* orthorhombic structure regardless of the atmospheric conditions but the super lattice reflections, annotated in Fig. 3.4.a, diminished in intensity in the samples exposed to 5% $\text{H}_2\text{-N}_2$, suggesting a decrease in orthorhombic distortion. The high-angle peaks of samples treated in 5% $\text{H}_2\text{-N}_2$ also show a very slight shift in peak position compared to those treated in air. This implies a nearly complete reduction of Fe^{4+} to Fe^{3+} in samples treated in 5% $\text{H}_2\text{-N}_2$, whereas samples treated in air became more oxidized with nominal iron concentration.

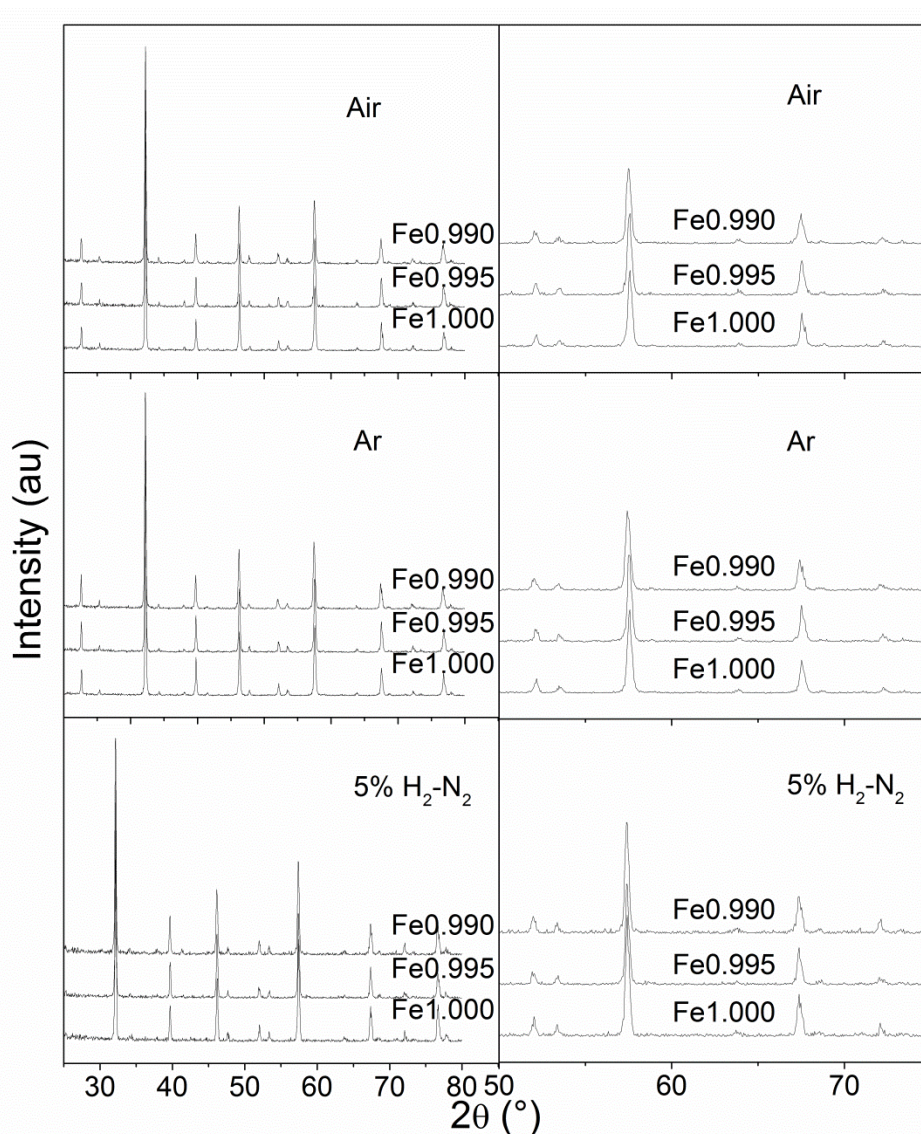


Fig. 3.4. XRD patterns for samples exposed to designated atmosphere at 1100°C. Column a) shows the entire XRD pattern with asterisk annotating some of the super-lattice reflections. Column b) shows the high angle data with drop lines to highlight the slight shift of peaks to lower angles with decreasing iron content.

The refined lattice parameters and unit-cell volumes of the heat-treated samples are also shown in Fig. 3.3 and listed in Table 3.1. Overall, neither the air, Fig 4-b, nor Ar, Fig. 3.4-c, caused any appreciable difference in the lattice parameters or the cell volume,

although there was a slight decrease in lattice parameter a of composition Fe10 when treated in Ar. When treated in Ar, it would be expected that small quantities of oxygen vacancies would form and that some the tetravalent iron would reduce to charge compensate for the oxygen vacancies. The reduction of iron should cause an increase in lattice parameters since the ionic radius of Fe^{3+} is greater than the ionic radius of Fe^{4+} , however with only a slight reduction taking place a relaxation in the lattice is likely to occur and compensate for the expansion caused by changes in the average iron radius.

After exposure to 5% $\text{H}_2\text{-N}_2$, the b and c lattice parameters of each composition increased measurably with a corresponding increase in the unit cell volume. Under the extremely reducing condition of 5% $\text{H}_2\text{-N}_2$, a substantial quantity of oxygen vacancies would be expected to form and would require the reduction of Fe^{4+} to Fe^{3+} . As mentioned above, the reduction of Fe^{4+} to Fe^{3+} would increase the average iron radius. However with a substantial amount of oxygen vacancy formation the Coulombic repulsion between cations and vacancy sites will cause an increase in unit cell volume, as is seen in all three samples and shown in Fig. 3.4-d.

Table 3.1 Lattice parameters and unit cell volumes of $\text{La}_{0.9}\text{Ca}_{0.1}\text{Fe}_y\text{O}_{3-\delta}$ compounds determined by XRD.

	[Fe]	a (Å)	b (Å)	c (Å)	Vol. (Å ³)
As-Prep.	1.000	5.561	7.826	5.537	241.0
	0.995	5.560	7.823	5.537	240.8
	0.990	5.567	7.823	5.534	241.0
Air	1.000	5.553	7.831	5.534	240.6
	0.995	5.550	7.823	5.535	240.3
	0.990	5.563	7.842	5.547	242.0
Ar	1.000	5.548	7.843	5.535	240.9
	0.995	5.544	7.836	5.535	240.5
	0.990	5.550	7.850	5.533	241.1
5% H ₂ -N ₂	1.000	5.565	7.847	5.547	242.2
	0.995	5.559	7.846	5.546	241.9
	0.990	5.562	7.846	5.549	242.1

3.3.2 Dilatometry

Dilatometry was used to observe the thermal expansion behavior and phase transformations, specifically the Néel transition and orthorhombic-to-rhombohedral transition temperatures, which we refer to as T_N and T_{OR} , respectively. The Néel transition is a magnetic transition from anti-ferromagnetic to paramagnetic and T_N is the temperature at which the transition occurs.²¹ The Néel transition of rare earth orthoferrites has been extensively studied. It has been shown that the transition is strongly dependent on the bond angle formed in the $\text{Fe}^{3+}\text{-O-Fe}^{3+}$ super-exchange that occurs along the long axis, which is the b direction in the case of the *Pnma* structure.^{9, 22, 23} The orthorhombic (*Pnma* symmetry)-to-rhombohedral ($R\bar{3}c$ symmetry) transition is a first-order reconstructive transition for lanthanum ferrite that occurs near 1000°C.²⁴

Figure 5 shows how the measured coefficients of thermal expansion (CTE) vary with temperature and atmosphere. Both T_N and T_{OR} were easily observed in the CTE data for those samples treated in air and Ar, as annotated in Fig. 3.5 and documented in Tables 2 and 3. In air, T_N decreased with increasing iron content from 400°C for Fe10 and to 345°C for Fe00. A similar trend was observed in samples treated in Ar as T_N was 435°C for Fe10 and 359°C for Fe00. A slight increase in T_N is expected as the atmospheric P_{O_2} is decreased, as it has been shown in previous studies that reducing atmospheres will cause the T_N of alkaline doped $LaFeO_3$ to become more like pure $LaFeO_3$ due to the reduction of Fe^{4+} to Fe^{3+} .²² Consistent with this prior observation, the Néel transition temperature of samples exposed to the more reducing 5% H_2-N_2 atmosphere were all found to be approximately 465°C, which is within the range of T_N values listed in literature for pure $LaFeO_3$.^{12, 23, 25} It is notable that the CTE peaks used to determine the T_N for Fe10 samples in air and Ar (Fig. 3.5) are not well defined, suggesting the transition is somewhat gradual. These transition ranges are annotated with both data sets shown in Fig. 3.5 using two arrows rather than one. For the purpose of this paper, we assume that the transition temperature corresponds to the maxima in CTE.

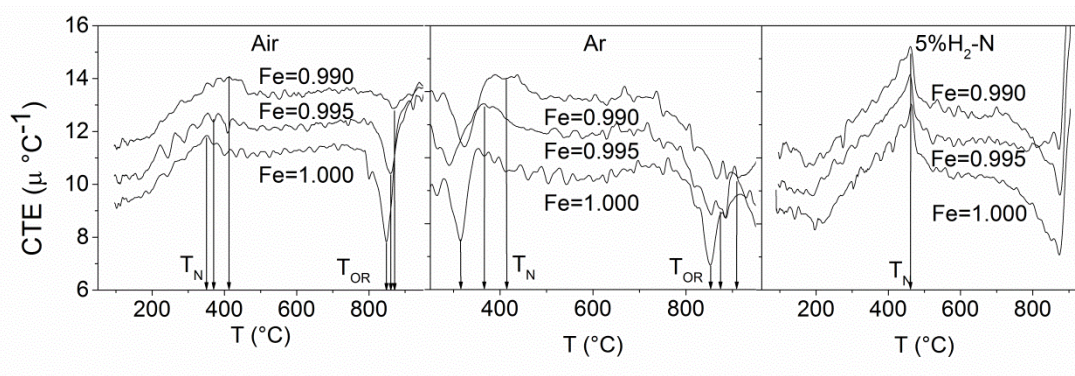


Fig. 3.5. Coefficient of thermal expansion (CTE) plots for all three atmosphere treatments with a +1 offset between compositions to more clearly show distinction

between compositions. The Néel transition (T_N) is annotated for each sample. The orthorhombic-to-rhombohedral transition is annotated for air and Ar runs but was not observable for the 5% H_2-N_2 treated samples. Different T_N s were observed for each composition in air- and Ar- treated samples. No difference in T_N was observed for any composition in the 5% H_2-N_2 treatment. All transition temperatures annotated here are listed in Tables 3.1 and 3.2.

Table 3.2. Orthorhombic-to-rhombohedral transition temperatures determined by dilatometry (DIL) and differential scanning calorimetry (DSC) in dry air and argon. The orthorhombic-to-rhombohedral transition measured in 5% H_2-N_2 occurred over a relatively wide temperature range and therefore could not be determined with precision by DSC or dilatometry.

Fe content	Air-DIL (°C)	Ar-DIL (°C)	Air-DSC (°C)	Ar-DSC (°C)
1.000	844	835	873	859
0.995	852	841	877	863
0.990	863	852	883	868

Table 3.3. Néel transition temperatures determined by dilatometry.

Fe content	Air (°C)	Ar (°C)	5% H_2-N_2 (°C)
1.000	345	359	468
0.995	360	370	465
0.990	400	435	464

With the introduction of calcium in to $LaFeO_3$, the long-range anti-ferromagnetic (AFM) ordering is expected to be disrupted by the formation of Fe^{4+} .^{9, 12} Unfortunately, there are no data in the open literature that have characterized the impact of B site deficiency on the Néel transition or T_N . As stated above in the discussion on XRD results, it is probable that the samples are effectively $La_{1-x}Ca_xFeO_3$ with x varying from 0.1 for Fe00 to approximately 0.09 for Fe10. If this were the case, then a higher T_N would be expected for Fe10 since the long-range AFM ordering would be less disrupted. If there were iron vacancies formed then the disruption to the long-range AFM ordering would be expected to increase and a lower T_N would be observed. Similarly, with iron vacancies,

there would be disruptions to the long-range AFM ordering for samples treated in 5% H₂-N₂; however, all three samples show the same T_N when completely reduced and are very near the T_N of pure LaFeO₃. This suggests that with complete reduction the long range AFM ordering is restored and all of the iron exists in a Fe³⁺ state, which is in agreement with the study by Grenier *et al.*²² and Komornicki *et al.*²³ on lanthanum ferrite behavior under reducing conditions.

The orthorhombic-to-rhombohedral transition temperature (T_{OR}) observed via dilatometry, shown in Fig. 3.5 and tabulated in Table 3.2, increased with Fe deficiency, a trend similar to that seen for T_N. The T_{OR} determined from dilatometry in air is 863°C for Fe10 and 844°C for Fe00 (Fig. 3.5.a); however, unlike the Néel transition, values of T_{OR} determined from dilatometry in Ar decreased rather than increased with increasing iron content and were 852°C and 835°C for Fe10 and Fe00, respectively. As stated above, the O-R transition is a first-order reconstructive transition. The bonding between octahedra in a fully oxidized sample, such as the samples treated in air, will generally be much stronger and uniform than the bonding between polyhedral in a reduced sample where bonds have been broken during oxygen-vacancy formation. As such, the reconstructive transformation temperature should be lower for reduced samples, which is observed.

3.3.3 TG-DSC/DTA

Both DSC and DTA analyses were performed on each composition as shown in Figs. 6. The orthorhombic-to-rhombohedral transformation temperatures can be seen in the endothermic peaks in the DSC data and are tabulated in Table 3.2. The T_{OR} was found to increase as the nominal iron content decreases and to decrease with decreasing P_{O₂}. There was no distinct peak to mark the O-R transition for the samples run in the DTA in

5% H₂-N₂, and instead the DTA curves showed a broad arcing shape from about 600 to 1100°C and increases in intensity from Fe00 to Fe10. This suggests that the O-R transition in highly reducing atmospheres is not a short, instantaneous transformation but a time-dependent process that takes place over a finite temperature range.

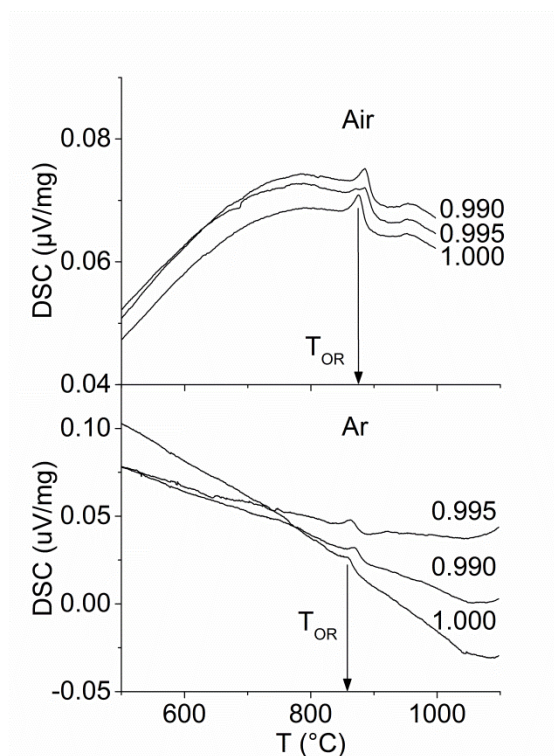


Fig. 3.6. T_{OR} in air and Ar was determined by the position of the endothermic peak in the DSC data and is annotated on the graph (left column). The right column shows the TG data for both air and Ar and has the Néel and O-R transitions annotated to show mass losses about the transitions.

The one hour isotherm used in heat treating the samples was not long enough for the samples to reach an equilibrium mass loss. Thus, the samples were held in a five hour isotherm at 1100°C and analyzed using TG-DTA in 5% H₂-N₂, shown in Fig. 3.7. The most telling information from exposure to 5% H₂-N₂ are the two distinct points of mass loss. The first is a small mass loss that occurs near T_N determined from dilatometry of

about -0.6% for non-stoichiometric samples and about -0.72% for stoichiometric samples (Fig. 3.8). The 0.6% mass loss corresponds to an oxygen δ of 0.09 and the 0.7% mass loss corresponds to an oxygen δ of 0.11. This makes the oxygen stoichiometry roughly 2.91 and 2.90 and provides more than enough vacancies for complete charge-compensation of calcium doping. The decreased loss of oxygen for Fe05 and Fe10 makes sense if there is a decreased amount of calcium and thus a decreased amount of Fe^{4+} to be reduced. The amount of oxygen lost in all three samples also requires the reduction of more Fe^{4+} than the amount that would be formed by calcium doping, implying that a slight amount of Fe^{3+} would need to be converted to Fe^{2+} . The presence of trace amounts of Fe^{2+} would cause some disruption to long range AFM ordering and explain why there is a slight decrease in T_N compared to pure LaFeO_3 .

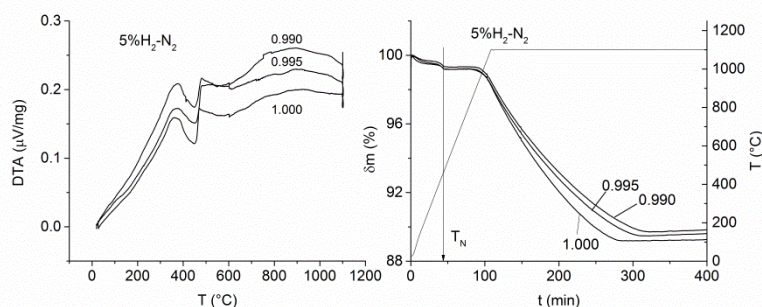


Fig. 3.7. TG-DTA data for samples treated in 5% $\text{H}_2\text{-N}_2$. Neither the Néel nor T_{OR} could be identified from the DTA data. A significant mass loss occurs and ends at the T_N determined from dilatometry and corresponds to a complete oxidation of Fe^{4+} to Fe^{3+} and some Fe^{3+} becoming Fe^{2+} .

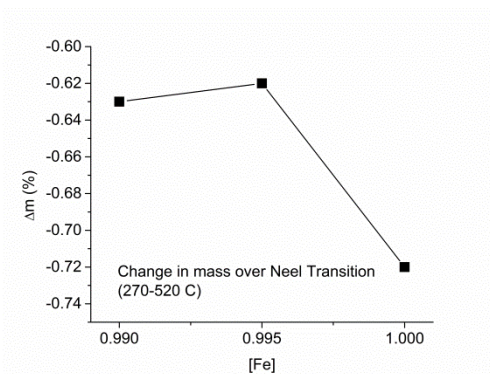


Fig. 3.8. Total mass loss over the Néel transition for samples in 5% H₂-N₂. The mass loss for non-stoichiometric samples suggests that the iron is already reduced and that the T_N for non-stoichiometric samples should be higher than for stoichiometric samples.

The most significant mass loss observed begins at around 900°C and continues into the isotherm until a critical mass loss and decomposition occurs. The mass loss, corresponding to oxygen loss, for each sample after decomposition is shown in Fig. 3.9 and decreases with decreasing nominal iron concentration, much like the oxygen loss near T_N. This same trend is shown in Fig. 3.10 where the time to complete decomposition is shown. With the consideration that iron deficiency produces a decreased concentration of calcium, the data shows that La_{1-x}Ca_xFeO₃ becomes more unstable with increasing calcium content due to the increased oxygen loss.

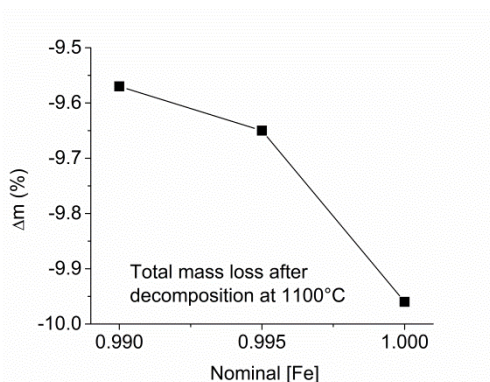


Fig. 3.9. Decomposition mass loss for samples in 5% H₂-N₂. The increasing magnitude of mass loss confirms that there was less oxygen available for non-

stoichiometric samples and there were more intrinsic oxygen defects in the samples compared to stoichiometric samples.

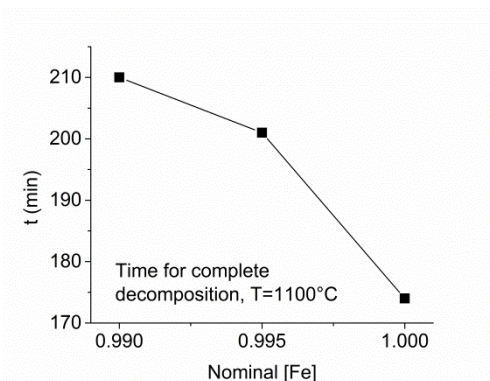


Fig. 3.10. Time to decomposition for samples held at 1100°C showing that non-stoichiometric samples are more stable and stoichiometric samples.

3.4 Conclusions

Phase transitions and impacts of non-stoichiometry in calcium doped lanthanum ferrite ($\text{La}_{0.9}\text{Ca}_{0.1}\text{Fe}_y\text{O}_{3-\delta}$) were successfully studied. It was found that the formation of significant B site vacancies is unlikely due to the high energy of the defect. Rather, the samples maintained a stoichiometric A to B ratio during preparation by limiting the number of A sites available and preferentially selecting lanthanum over calcium to fill the A sites. Thus, nominal iron deficiency during preparation equates to a decrease in calcium content for $\text{La}_{0.9}\text{Ca}_{0.1}\text{Fe}_y\text{O}_{3-\delta}$. As seen in previous literature, an increase in calcium content causes a decrease in both the Néel transition temperature and the orthorhombic-to-rhombohedral transition temperature due at least in part to a higher concentration of Fe^{4+} . Using DSC and dilatometry, this was observed as both transition temperatures were shown to decrease increases in nominal iron content and confirmed that there is preferential selection of lanthanum over calcium during preparation. In addition, it was confirmed that reducing conditions increases the Néel transition temperature and decreases the orthorhombic-to-rhombohedral transition temperature. It

was also shown that oxygen-vacancy formation can be controlled by the exposure to reducing atmospheres during heating and that oxygen loss is accompanied by the reduction of Fe^{4+} to Fe^{3+} . When exposed to highly reducing atmospheres, such as 5% H_2 - N_2 , the Fe^{4+} becomes entirely reduced to Fe^{3+} at the Néel transition and further release of oxygen is negligible until 900°C. Further oxygen loss occurs after 900°C and is most significant for samples with higher calcium concentrations. In addition, samples with lower calcium concentrations also took longer to reach a critical oxygen reduction and decomposition.

3.5 Acknowledgements

This research was partially supported by the NRC-38-08-955 nuclear materials fellowship. The authors are grateful to Patrick Price and Jordan Chess for their contributions to this research.

3.6 Author Justifications

The research presented in this publication was carried out and authored by Geoffrey L. Beausoleil II as partial fulfillment of the requirements for a Master of Science degree in Materials Science and Engineering at Boise State University. Contributions to procedures, the carrying out of characterization, and critical feedback were made by Patrick Price and Jordan Chess. In addition, Dr. Darryl Butt and Dr. Alex Punnoose made significant contributions toward this work in terms of providing the necessary guidance, materials, equipment, and funding for the success of the experiments presented.

3.7 References

1. M. F. Carolan, P. N. Dyer, R. M. P. H. van Doorn, R. A. Cutler, and D. P. Butt, "Ion Transport Membranes for Syngas Production," Patent # 6492290, United States of America 2003.
2. P. N. Dyer, M. F. Carolan, D. P. Butt, R. M. P. H. van Doorn, R. A. Cuter, and K. D. Gourley, "Mixed Conducting Membranes for Syngas Production," Patent # 2001295502, Australia 2005.
3. P. Ciambelli, S. Cimino, L. Lisi, M. Faticanti, G. Minelli, I. Pettiti, and P. Porta, "La, Ca and Fe Oxide Perovskites: Preparation, Characterization and Catalytic Properties for Methane Combustion," *Applied Catalysis B-Environmental*, **33** [3] 193-203 (2001).
4. K. Vidal, L. Rodriguez-Martinez, L. Ortega-San-Martin, M. No, T. Rojo, and M. Arriortua, "Effect of the A Cation Size Disorder on the Properties of an Iron Perovskite Series for Their Use as Cathodes for SOFCs," *Fuel Cells*, **11** [1] 51-58 (2011).
5. H. Taguchi, Y. Masunaga, K. Hirota, and O. Yamaguchi, "Synthesis of Perovskite-type $\text{La}_{1-x}\text{Ca}_x\text{FeO}_3$ ($0 \leq x < 0.2$) at low temperature," *Materials Research Bulletin*, **40** [5] 773-80 (2005).
6. K. J. Yoon, P. A. Zink, S. Gopalan, U. B. Pal, and L. R. Pederson, "Defect Chemistry and Electrical Properties of $\text{La}_{0.8}\text{Ca}_{0.2}\text{FeO}_{3-d}$," *Journal of the Electrochemical Society*, **156** [7] B795-B800 (2009).

7. U. F. Vogt, P. Holtappels, J. Sfeir, J. Richter, S. Duval, D. Wiedenmann, and A. Züttel, "Influence of A-Site Variation and B-Site Substitution on the Physical Properties of (La,Sr)FeO₃ Based Perovskites," *Fuel Cells*, **9** [6] (2009).
8. S. E. Dann, D. B. Currie, M. T. Weller, M. F. Thomas, and A. D. Alrawwas, "The Effect of Oxygen Stoichiometry on Phase-Relations and Structure in the System La_{1-x}Sr_xFeO_{3-δ}," *Journal of Solid State Chemistry*, **109** [1] 134-44 (1994).
9. J. M. Hudspeth, G. A. Stewart, A. J. Studer, and D. J. Goossens, "Crystal and Magnetic Structures in Perovskite-related La_{1-x}Ca_xFeO₃ (x=0.2, 0.33)," *Journal of Physics and Chemistry of Solids*, **72** [12] 1543-47 (2011).
10. A. N. Nadeev, S. V. Tsybulya, V. D. Belyaev, I. S. Yakovleva, and L. A. Isupova, "Weakly Bound Oxygen and its Role in Stability of Solid Solutions La_{1-x}Sr_xFeO₃," *Journal of Structural Chemistry*, **49** [6] 1077-83 (2008).
11. M. Mori, Y. Hiei, N. Sammes, and G. Tompsett, "Thermal-expansion behaviors and mechanisms for Ca- or Sr-doped lanthanum manganite perovskites under oxidizing atmospheres," *Journal of the Electrochemical Society*, **147** [4] 1295-302 (2000).
12. G. L. Beausoleil II, P. Price, D. Thomsen, A. Punnoose, R. Uvic, S. Misture, and D. P. Butt, "Thermal Expansion of Alkaline-Doped Lanthanum Ferrite Near the Néel Temperature", accepted for publication in *J. Amer. Cer. Soc.*, 2013.
13. B. H. Toby, "EXPGUI, a graphical user interface for GSAS," *J. Appl. Cryst.*, **34** 210-13 (2001).
14. A. C. Larson and R. B. Von Dreele, "General Structure Analysis System (GSAS)," pp. 86-748. Edited by LAUR, Los Alamos National Laboratory, 1994.

15. M. Mori and Z. W. Wang, "Pore Formation During Sintering Process of $(\text{Sr}_{0.9}\text{La}_{0.1})_{1-x}\text{Ti}_{1-y}\text{O}_3$ Perovskites ($x, y=0, 0.04$) Synthesized by the Citric Acid Method," *Electrochemistry*, **78** [11] 896-99 (2010).
16. S. N. Ruddlesden and P. Popper, "The Compound $\text{Sr}_3\text{Ti}_2\text{O}_7$ and Its Structure," *Acta Crystallographica*, **11** [1] 54-55 (1958).
17. S. N. Ruddlesden and P. Popper, "New Compounds of the K_2NiF_4 Type," *Acta Crystallographica*, **10** [8] 538-40 (1957).
18. B. Beznosikov and K. Aleksandrov, "Perovskite-like crystals of the Ruddlesden-Popper series," *Crystallography Reports*, **45** [5] 792-98 (2000).
19. R. Grimes, "Database of Ionic Radii" (2012), Imperial College. Accessed on: 17 Jan, 2012. Available at <http://abulafia.mt.ic.ac.uk/shannon/ptable.php>
20. M. Mori, Z. W. Wang, T. Itoh, S. Yabui, K. Murai, and T. Moriga, "A-Site and B-Site Non-stoichiometry and Sintering Characteristics of $(\text{Sr}_{1-x}\text{La}_x)_{1-y}\text{Ti}_{1-z}\text{O}_3$ Perovskites," *Journal of Fuel Cell Science and Technology*, **8** [5] 4 (2011).
21. G. F. Dionne, *Magnetic oxides*; Ch. Chapter. Edited. Springer: New York, 2009.
22. J. C. Grenier, L. Fournes, M. Pouchard, and P. Hagenmuller, "Mossbauer Resonance Studies on the $\text{Ca}_2\text{Fe}_2\text{O}_5$ - LaFeO_3 System," *Materials Research Bulletin*, **17** [1] 55-61 (1982).
23. S. Komornicki, L. Fournes, J. C. Grenier, F. Menil, M. Pouchard, and P. Hagenmuller, "Investigation of Mixed Valency Ferrites $\text{La}_{1-x}\text{Ca}_x\text{FeO}_{3-y}$ ($0 < x < 0.50$) With the Perovskite Structure," *Materials Research Bulletin*, **16** [8] 967-73 (1981).

24. S. M. Selbach, J. R. Tolchard, A. Fossdal, and T. Grande, "Non-linear Thermal Evolution of the Crystal Structure and Phase Transitions of LaFeO_3 Investigated by High Temperature X-ray Diffraction," *Journal of Solid State Chemistry*, **196** 249-54 (2012).
25. T. Peterlinneumaier and E. Steichele, "Antiferromagnetic Structure of LaFeO_3 From High-Resolution ToF Neutron-Diffraction," *Journal of Magnetism and Magnetic Materials*, **59** [3-4] 351-56 (1986).